





RESEARCH ARTICLE | DECEMBER 27 2023

# Particle dynamics in vertical vibration-driven immersed granular systems: A study with resolved computational fluid dynamics-discrete element method

Chi Wang (王驰) ; Lubin Wei (韦鲁滨) ; Yi An (安翼)  

 Check for updates

*Physics of Fluids* 35, 123343 (2023)

<https://doi.org/10.1063/5.0179357>



08 April 2024 03:15:08



## APL Energy

### Latest Articles Online!

**Read Now**



# Particle dynamics in vertical vibration-driven immersed granular systems: A study with resolved computational fluid dynamics-discrete element method

Cite as: Phys. Fluids **35**, 123343 (2023); doi: 10.1063/5.0179357

Submitted: 1 October 2023 · Accepted: 6 December 2023 ·

Published Online: 27 December 2023






View Online



Export Citation



CrossMark

Chi Wang (王驰),<sup>1,2</sup>  Lubin Wei (韦鲁滨),<sup>1</sup>  and Yi An (安翼),<sup>2,3,a)</sup> 

## AFFILIATIONS

<sup>1</sup>School of Chemical and Environmental Engineering, China University of Mining and Technology (Beijing), Beijing 100083, China

<sup>2</sup>Key Laboratory for Mechanics in Fluid Solid Coupling Systems, Institute of Mechanics, Chinese Academy of Sciences, Beijing 100190, China

<sup>3</sup>School of Engineering Science, University of Chinese Academy of Sciences, Beijing 100049, China

<sup>a)</sup> Author to whom correspondence should be addressed: [anyi@imech.ac.cn](mailto:anyi@imech.ac.cn)

## ABSTRACT

Vibration-driven immersed granular systems (VIGSs) are ubiquitous in nature and industry. However, particle dynamics in 3D VIGSs is hard to obtain directly from experiments. The resolved Computational Fluid Dynamics-Discrete Element Method (CFD-DEM) is introduced to study a cylindrical VIGS subjected to vertical vibration focusing on particle dynamics. A Voronoi-weighted Gaussian interpolation (VWGI) method is used to convert the discrete particle information into a continuous field. The VWGI method enables the estimation of the continuous field for granular systems, especially for those with large-scale non-uniformity and heterogeneity particle distribution in local cells. The results show that the periodic variation of the system's kinetic energy is caused by the collision between the lower particles and the vibrating wall, and the particle kinetic energy decreases with height rising. A velocity spatial structure of convection, moving from the cylinder center to the sidewall, is observed in both immersed and dry systems away from the bottom. Vibration-driven particles can exhibit a similar flow structure to natural convection. Compared to the dry system, the convection strength and momentum transfer in the VIGS are higher, while the momentum diffusion is lower. The fluid restrains the particle energy acquisition and enhances the energy dissipation of the "heated" particles, while the formation of the fluid convection benefits the particle convection directionality. This resolved CFD-DEM study with the VWGI method provides useful results of the particle dynamics in VIGSs, which could provide guidance for some practical applications in minerals processing involving vibration-driven immersed granular systems.

Published under an exclusive license by AIP Publishing. <https://doi.org/10.1063/5.0179357>

## I. INTRODUCTION

Immersed granular systems, encompassing phenomena like debris flow,<sup>1</sup> landslides,<sup>2</sup> and seismic liquefaction,<sup>3</sup> pose significant threats to people's life and property safety. Furthermore, these systems find extensive applications across various industrial domains, including chemical processes,<sup>4,5</sup> and mineral processing.<sup>6,7</sup> The fundamental particle dynamics within granular systems, such as those occurring in debris flow, are primarily governed by granular shearing, a process that can be deconstructed into shearing and vibration components.<sup>8,9</sup> Extensive research has been devoted to understanding the shearing mechanism, particularly in dry granular systems,<sup>10,11</sup> resulting in the establishment of numerous macro-phenomenological models

grounded in rheological principles.<sup>12-14</sup> The rheological behavior of immersed particles has also emerged as a significant area of study. In this context, the influence of the surrounding liquid is incorporated by introducing viscosity into the inertia number. Consequently, several phenomenological models have been developed to characterize the motion of particles immersed in a fluid medium.<sup>15-18</sup> In contrast to shearing systems, the development of macro-phenomenological theories for vibration-driven granular systems (VGSs) remains a burgeoning field. The predominant focus of previous studies has centered on vibration-driven dry granular systems (VDGSs).<sup>19,20</sup> A substantial body of literature has explored fundamental particle dynamics, encompassing granular temperature, velocity, and volume fraction.<sup>21-23</sup>

Studies have also examined the spatial distribution of these dynamic features and established corresponding scaling laws.<sup>24,25</sup> Notably, investigations have delved into the impact of interstitial liquid viscosity on granular temperature.<sup>26</sup> Another prominent research area revolves around the phase diagram of granular motion.<sup>27–29</sup> This phase diagram hinges on variables such as vibration intensity, particle diameter, and granular layer height, delineating the sequence in which distinct phases manifest as fluidization progresses. These phases encompass the bouncing bed, undulations, granular Leidenfrost effect, convection rolls, and granular gas.<sup>30</sup> Furthermore, extensive attention has been devoted to energy dissipation within the system,<sup>31,32</sup> as well as the dynamics of particle mixing and separation.<sup>33–36</sup> However, the exploration of particle dynamics within vibration-driven immersed granular systems (VIGSs) remains in its nascent stages, characterized by a paucity of detailed descriptions pertaining to basic particle dynamic features. This endeavor could provide guidance for some practical applications involving vibration-driven immersed granular systems, such as the design of novel vibrating screens in minerals processing.

Particle motion within 2D granular systems can be readily observed and analyzed using high-speed cameras.<sup>37,38</sup> However, when it comes to 3D granular systems with particle occlusion, capturing these motions becomes a challenging work. X-ray imaging techniques have proven effective for studying slow-motion processes within 3D granular systems.<sup>39</sup> Nevertheless, the dynamic behavior of particles intensifies when subjected to high-intensity vibrations, making it exceedingly difficult to investigate particle dynamics in 3D VIGSs using current experimental methodologies. Computational Fluid Dynamics-Discrete Element Method (CFD-DEM) simulations have emerged as a valuable tool for investigating granular-fluid systems, capitalizing on the DEM to compute particle interactions while also accounting for fluid-particle interactions.<sup>40–44</sup> It is important to note that the unresolved CFD-DEM approach relies on empirical formulas from prior studies to compute fluid-particle interactions, limiting its ability to uncover fundamental mechanisms underlying the fluid-particle interaction process.<sup>45–47</sup> In contrast, the resolved CFD-DEM method employs fluid cells significantly smaller than particles, enabling a detailed resolution of the fluid field around each particle and the individual calculation of forces on particles.<sup>48–50</sup> However, a fundamental challenge lies in defining the moving boundary of the particles. As a fixed mesh approach, the Fictitious Domain Method (FDM) introduces boundary conditions as force terms into the Navier–Stokes equations, thereby correcting velocity and pressure fields accordingly.<sup>51–54</sup> It is noteworthy that the lattice Boltzmann method (LBM) is alternative for fluid modeling,<sup>55</sup> and coupling between LBM and DEM has been developed in recent decades.<sup>56–58</sup> Its advantage lies in the simplicity of its governing equations compared to traditional CFD methods, exhibiting excellent performance in parallel computing.<sup>55,59</sup> However, LBM-DEM still requires more improvement on handling problems with complex boundary due to limited spatial resolution. In this study, the conventional resolved CFD-DEM method proposed by Hager *et al.*<sup>60</sup> was applied for studying VIGSs.

A comprehensive understanding of particle dynamics necessitates the transformation of discrete particle information into a continuous field. Traditional methods involve dividing the research space into numerous uniformly sized cells, wherein discrete data within each cell over a recorded duration are collected and averaged.<sup>21,25</sup> The resultant averaged value is considered the continuous value at the center of each

cell. However, in the classic approach, particles within cells are assigned uniform weights, disregarding both their distance from the cell center and the heterogeneity of particle distribution within the cell. Consequently, even a minor fluctuation in particle numbers within a cell, on the order of a few percent, can substantially impact the accuracy of the averaged flow field, undermining fidelity. Gaussian interpolation, a technique used to estimate values between known data points in a dataset, offers a promising alternative.<sup>61</sup> This method assigns weights to neighboring data points based on their proximity to the point of interpolation and utilizes them to compute the estimated value at the desired location. Weight calculations often employ the Gaussian function, with closer data points receiving higher weights and farther ones receiving lower weights.<sup>62</sup> However, traditional Gaussian interpolation normalizes the cumulative weight of neighboring points using a nonobjective normalization factor, a limitation particularly evident when dealing with large-scale non-uniformity and the heterogeneity particle distribution in local cells. Consequently, it is essential to consider the spatial distribution characteristics of known data points to ensure the rationality of surrounding point weights. To address this challenge, the volume occupied by each particle serves as a quantification of particle heterogeneity, allowing it to be integrated into the Gaussian function for the correction of surrounding particle weights.<sup>63,64</sup> Furthermore, this discrete particle volume fraction can be calculated utilizing this volume. Voronoi cells prove invaluable for precisely characterizing the volume fraction of each particle, as their volume closely mirrors the volume occupied by individual particles.<sup>65–68</sup>

This paper presents an investigation employing the resolved CFD-DEM to simulate a cylindrical VIGS. We employ the Voronoi-weighted Gaussian interpolation (VWGI) method to make continuous analysis of particle dynamics. In Sec. II, we provide a detailed exposition of the resolved CFD-DEM simulation method and the VWGI method. We conduct a mesh independence test and scrutinize the normalization of the cumulative weight of neighboring points. Section III elucidates the temporal variation and spatial distribution of the particle kinematics within the VIGS, which are then compared to their counterparts in the VDGS. In Sec. IV, we analyze convection strength, momentum transfer, and diffusion in both particle systems and draw analog of the convection in both immersed and dry particle systems to natural convection. In Sec. V, we delve into an exploration of the fluid's impact on particle movement within the VIGS. Finally, the paper concludes with a summary of key findings and remarks.

## II. METHODOLOGY

### A. CFD-DEM simulation

#### 1. Governing equations

The governing equations are written as follows:<sup>69</sup>

$$\rho \frac{\partial \mathbf{U}}{\partial t} + \rho(\mathbf{U} \cdot \nabla)\mathbf{U} = -\nabla p + \mu \Delta \mathbf{U} + \rho \mathbf{g} \quad \text{in } \Omega, \quad (1)$$

$$\nabla \cdot \mathbf{U} = 0 \quad \text{in } \Omega, \quad (2)$$

$$\mathbf{U} = \mathbf{U}_\Gamma \quad \text{on } \Gamma, \quad (3)$$

$$\mathbf{U}(x, t = 0) = \mathbf{U}_0(x) \quad \text{in } \Omega, \quad (4)$$

$$\mathbf{U} = \mathbf{U}_p \quad \text{on } \Omega_s, \quad (5)$$

$$\boldsymbol{\sigma}_f \cdot \hat{\mathbf{n}} = \mathbf{s}_\Gamma \quad \text{on } \Gamma_s, \quad (6)$$

$$m_p \frac{dU_p}{dt} = m_p \mathbf{g} + \mathbf{f}_f + \sum \mathbf{f}_c, \quad (7)$$

$$I_p \frac{d\omega_p}{dt} = T_f + \sum T_c, \quad (8)$$

where  $\Omega_f$  is the fluid domain,  $\Omega_s$  is the particle phase,  $\Omega = \Omega_f \cup \Omega_s$ ,  $\Gamma$  is the boundary of  $\Omega$ , and  $\Gamma_s$  is the interface between fluid and particle.  $\mathbf{U}$  represents the velocity,  $p$  is the pressure,  $t$  is the time,  $\rho$  is the density,  $\mathbf{g}$  is the gravitational acceleration with magnitude  $9.81 \text{ m/s}^2$ ;  $\mathbf{U}_\Gamma$  is the velocity on  $\Gamma$  and  $\mathbf{U}_p$  is the velocity on  $\Omega_s$ ,  $\boldsymbol{\sigma}_f$  denotes the stress tensor of the fluid,  $\hat{\mathbf{n}}$  is the outer normal vector of the particle,  $\mathbf{s}_{\Gamma_s}$  is the traction vector of the fluid, acting on the particle,  $m_p$  is the mass of the particle,  $\mathbf{f}_f$  represents the fluid force on the particle,  $\sum \mathbf{f}_c$  is denoted as the force caused by the particle–particle/wall interactions,  $\omega_p$  is the angular velocity of the particle,  $I_p$  is the particle’s moment of inertial,  $T_f$  is hydrodynamic torque, and  $\sum T_c$  is the torque due to the particle–particle/wall interactions.

Equations (1) and (2) are the motion and continuity equations for the whole domain; Eq. (3) represents the Dirichlet boundary condition; Eq. (4) is the initial condition of the computation domain; Eq. (5) is used to transfer the rigid velocity on the fluid velocity; Eq. (6) represents the stress between the fluid and solid; Eqs. (7) and (8) are used to catch the rigid motion and rotation, respectively.

$\mathbf{f}_f$  can be calculated as follows:

$$\mathbf{f}_f = \mathbf{f}_f^\sigma + \mathbf{f}_f^b, \quad (9)$$

$$\int_{\Gamma_s} \boldsymbol{\sigma}_f \cdot \hat{\mathbf{n}} = \int_{\Gamma_s} \mathbf{s}_{\Gamma_s} = \mathbf{f}_f^\sigma, \quad (10)$$

$$\mathbf{f}_f^b = \rho \mathbf{g} V_p, \quad (11)$$

where  $\mathbf{f}_f^\sigma$  represents the stress force of fluid acted on particles.  $\mathbf{f}_f^b$  is the buoyant force of fluid calculated by Archimedes principle, and  $V_p$  is the volume of the particle.

The DEM model utilized in our research adopts the soft-sphere approach, allowing for particle and boundary overlaps within the system. Interactions between particles and walls, as well as among particles, are computed using the non-linear spring-dashpot Hertz–Mindlin particle contact model, extensively documented in previous studies.<sup>29,49,70</sup>

### 2. Method implementation

The resolved CFD-DEM method is implemented within the open-source framework of CFDEMcoupling (<https://github.com/CFDEMproject/CFDEMcoupling-PUBLIC>), which provides an interface between OpenFOAM-5 (<https://openfoam.org>) and the DEM software LIGGGHTS (<https://www.cfdem.com>).

The simulation procedure of this method in one iteration step is shown in Fig. 1 and is explained as follows:

1. The DEM information at time  $t$  is used to acquire the particle occupied cells, and  $\mathbf{f}_f$  at time  $t$  is calculated.
2.  $\mathbf{f}_f$  is introduced into the DEM inner loop to calculate the particle information at the end of the one iteration step  $t + \Delta t$ ,  $\Delta t$  is  $n$

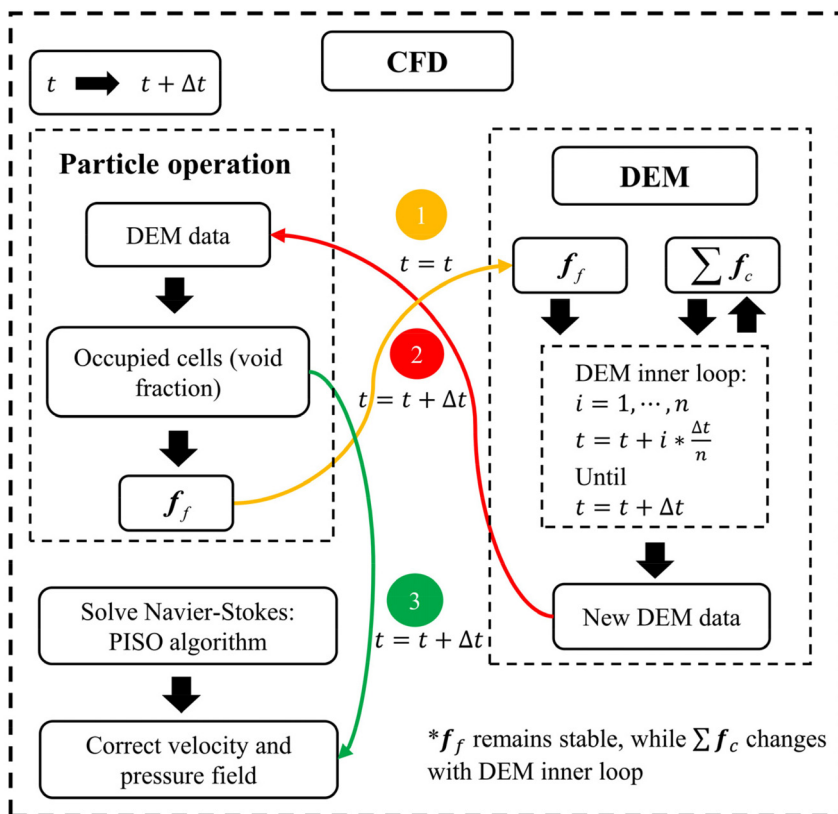
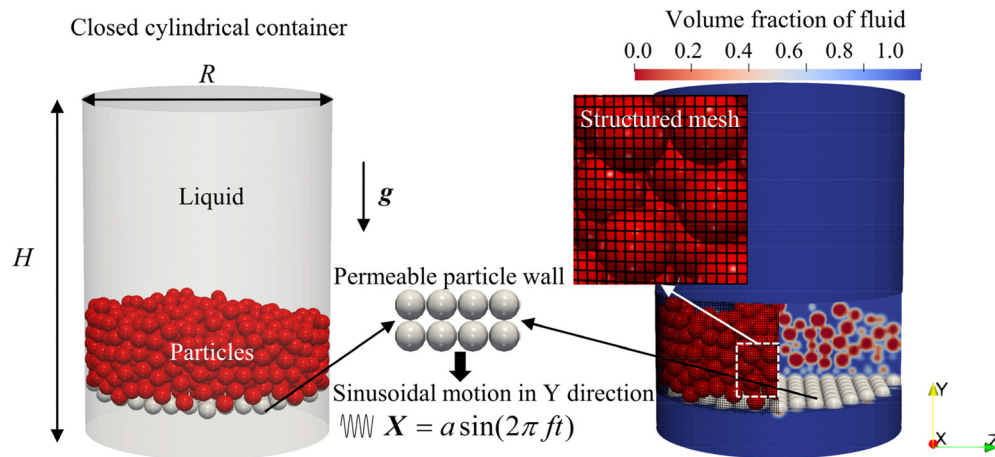


FIG. 1. CFD-DEM simulation procedure in one iteration step.  $\mathbf{f}_f$  represents the fluid force on the particle,  $\sum \mathbf{f}_c$  is denoted as the force due to the particle–particle/wall interactions.



**FIG. 2.** The VIGS for simulation. A sealed cylinder filled with liquid, where particles (red particles) are placed atop a permeable vibrating wall (white particles) allowing only liquid passage. After the simulation initiation, the vibrating wall undergoes standard sinusoidal motion in the Y-direction. The black grid is the structured mesh of the fluid domain. The nephogram shows the particle's boundary captured by the resolved CFD-DEM method.

times the iteration step length of the DEM inner loop, and  $n$  must be a positive integer.

- The particle occupied cells are updated to time  $t + \Delta t$ . Meanwhile, the whole domain uncorrected fluid field at time  $t + \Delta t$  is solved in the PISO loop. Combining the above information, the corrected fluid field is refreshed to time  $t + \Delta t$ . One iteration step is accomplished.

### 3. Case configuration

In this study, we have opted for a VIGS, as depicted in Fig. 2, to serve as a fundamental representation of various scenarios. This model embodies the concept of a constrained, axially symmetric, three-dimensional cell subjected to gravitational forces. Within a sealed cylindrical container, the interior is filled with a liquid medium. Particles are placed atop a permeable vibrating wall allowing only liquid passage. After the simulation initiation, the vibrating wall

undergoes standard sinusoidal motion in the vertical (Y) direction, which can be expressed as follows:

$$X = a \sin(2\pi ft), \tag{12}$$

where  $X$  represents the displacement of the vibrating wall in the Y-direction and  $a$  and  $f$  are the vibrating amplitude and frequency, respectively.

We employ LIGGGHTS code to simulate the VDGS under the same condition. A comprehensive listing of the specific parameter configurations utilized in the simulations is provided in Table I.

Note that the particles constructing the vibrating wall are the same as the research particles. Other walls' mechanical properties are the same as the particles.

According to our validation, when  $\Delta t_f$  is reduced to  $1.5 \times 10^{-4}$  s, the simulation results do not significantly change further with decreasing CFD time step. Considering the simulation accuracy and cost, we have determined the CFD time step of  $1.5 \times 10^{-4}$  s.

**TABLE I.** Parameters setting of the simulation.

Computational domain/CFD/coupling settings		DEM settings	
Parameters	Setting	Parameters	Setting
Cylinder height $H$ (m)	0.2	Particle diameter $d_p$ (m)	0.01
Cylinder radius $R$ (m)	0.075	Particle density $\rho_p$ (kg/m <sup>3</sup> )	2500
Fluid density $\rho_f$ (kg/m <sup>3</sup> )	1000	Particle number	800
Fluid kinematic viscosity $\nu_f$ (m <sup>2</sup> /s)	$1 \times 10^{-6}$	Youngs modulus $E$ (kg/m s <sup>-2</sup> )	$5 \times 10^7$
Boundary	Static without slip	Poisson's ratio	0.45
Mesh scale $M_s$ (m)	$1.25 \times 10^{-3}$	Coefficient restitution	0.95
Mesh number	2 959 308	Coefficient friction	0.5
CFD time step $\Delta t_f$ (s)	$1.5 \times 10^{-4}$	Coefficient rolling friction	0.03
Coupling interval	$15 \Delta t_p$	Vibration amplitude $a$ (m)	0.01
Paralleling processors number	256	Vibration frequency $f$ (Hz)	50
		DEM time step $\Delta t_p$ (s)	$1 \times 10^{-5}$

$\Delta t_p$  can be estimated by the particle collision time  $t_c$

$$t_c = 2.868 \left( \frac{m_p^2}{0.5 E d_p U_c} \right)^{1/5}, \quad (13)$$

where  $U_c$  is the feature collision velocity of the particles.

$U_c$  is set the same as the vibration velocity amplitude to make the estimation.  $\Delta t_p$  is established to be less than one-tenth of  $t_c$  to effectively capture particle collisions and uphold computational accuracy.

#### 4. Mesh independence test

Prior to commencing the simulations, it is imperative to conduct a mesh independence verification, as an excessively large mesh size can lead to obvious alterations in the occupied cells by particles during each iteration, significantly compromising the accuracy of our calculations.<sup>69</sup>

To determine an appropriate mesh size, we examine the probability density distributions of the particle kinetic energy ( $E_K$ ) and the magnitude of the total force acting on particles ( $\|F\|$ ), and the results

are depicted in Figs. 3(a) and 3(b). The simulation duration is set to 0–7 s, and the analysis duration for variables' probability density distributions is set to 3–7 s. To facilitate the clear representation of probability density distributions for multiple data groups, we employ lines connecting the midpoints of each bin instead of histograms. From Fig. 3(a), it is evident that when the grid size is  $1/3 d_p$ , the proportion of high kinetic energy particles is notably lower compared to that of the  $1/10 d_p$  grid size. As the grid size decreases to  $1/5 d_p$ , the aforementioned difference diminishes, yet the proportion of intermediate kinetic energy particles exhibits a significant variance from the  $1/10 d_p$  grid size. Upon further reduction in the grid size to  $1/8 d_p$ , the probability density distribution of particle kinetic energy aligns closely with that of the  $1/10 d_p$  grid size. From Fig. 3(b), it can be observed that the probability density of  $\|F\|$  remains relatively constant after the grid size decreases to  $1/8 d_p$ , showing no significant change with further reduction in grid size.

We calculate cumulative absolute difference ( $\sum |\Delta P|$ ) between the probability represented by each bin in the computed probability density distribution under different grid sizes and the trustworthy results, enabling a quantitative description of grid independence

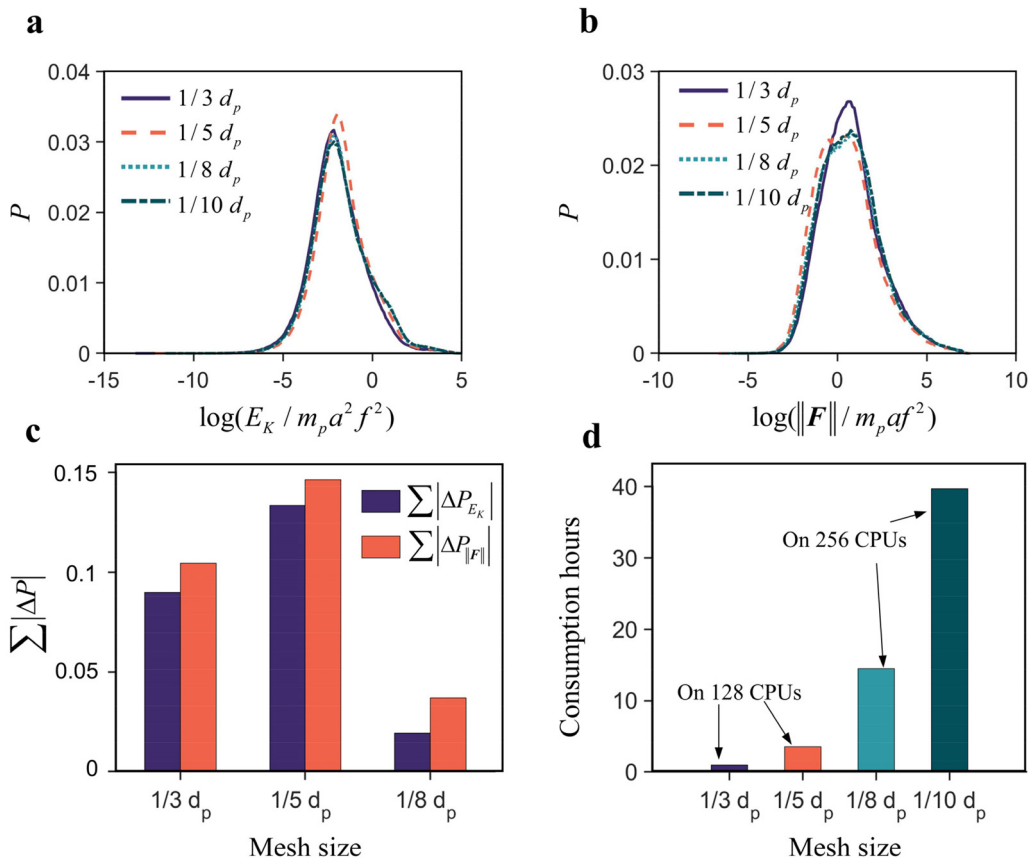


**FIG. 3.** Mesh independence test. Four sets of structured mesh with different sizes ( $1/3 d_p$ ,  $1/5 d_p$ ,  $1/8 d_p$ ,  $1/10 d_p$ ) are compared. (a) The probability density distributions of the particle kinetic energy ( $E_K$ ) with different grid sizes. (b) The magnitude of the total force acting on particles ( $\|F\|$ ) with different grid sizes. Note that the line connecting the midpoints of each bin, with width of 0.1, is used to replace the histogram. The duration for analysis is 3–7 s. (c) The cumulative absolute difference ( $\sum |\Delta P|$ ) between the probability represented by each bin in the computed probability density distribution under different grid sizes and the trustworthy results. The computation results from the  $1/10 d_p$  grid size are used as the trustworthy results. (d) Time consumption under different grid size. Simulation duration is 0–7 s.

08 April 2024 03:15:08

assessment. The computational results from the  $1/10 d_p$  grid size is used as the trustworthy reference to compute the  $\sum |\Delta P|$  of cases with different grid sizes, as shown in Fig. 3(c). In Fig. 3(c), the  $\sum |\Delta P|$  of the  $1/8 d_p$  grid size is notably smaller than the other grid sizes, providing a clearer indication that at a grid size of  $1/8 d_p$ , the computational accuracy is generally acceptable. Figure 3(d) demonstrates that the computational cost for the  $1/10 d_p$  grid size is notably higher than that for the  $1/8 d_p$  grid size. When using the same number of central processing units (CPUs), the computational time for the  $1/10 d_p$  grid size exceeds that of the  $1/8 d_p$  grid size by more than twice, attributed to the increased number of grid points and the reduction in CFD time step. Consequently, in this study, we opt for a grid size of  $1/8 d_p$  to strike a balance between computational accuracy and cost.

Considering the case configuration is fully located in the validated zone of the CFDEMcoupling code with extensive application and detailed validation,<sup>60,71,72</sup> the validation process and the results are omitted for the sake of space.

### B. Voronoi-weighted Gaussian interpolation method

The interpolation process relies on the Gaussian interpolation function, which can be expressed as

$$f(X_i) = \sum_{j=1}^{N_i} y_{ij} W_{ij}, \tag{14}$$

$$W_{ij} = \frac{1}{(2\pi)^{1.5} h_i^3} e^{-\frac{r_{ij}^2}{2h_i^2}}. \tag{15}$$

Here,  $f(X_i)$  signifies the estimated value at the interpolation point  $X_i$ ,  $y_{ij}$  represents the corresponding value of the known data point  $x_{ij}$  in the vicinity of  $X_i$ , and  $N_i$  denotes the number of neighboring points within the calculation radius  $h_i$  of  $X_i$ . The weight  $W_{ij}$  for each data point  $x_{ij}$  is determined by Eq. (14), with the condition that the Euclidean distance  $r_{ij}$  between  $X_i$  and  $x_{ij}$  does not exceed the specified calculation radius.

To enhance the accuracy of the interpolation, we incorporate point feature volume, which is obtained using the open-source software Voro++ and the Qhull algorithm,<sup>65,73</sup> to adjust the weights of surrounding points. The improved weight function is expressed as

$$W_{ij} = \frac{Vo_{ij}}{V_i} e^{-\frac{r_{ij}^2}{2h_i^2}}. \tag{16}$$

Here, the point feature volume ( $Vo_{ij}$ ) is normalized by the volume of the support zone ( $V_i$ ). A graphical representation of the VWGI method is presented in Fig. 4.

To mitigate non-uniformities in the original data at a large scale, we propose a  $h_i$  self-adaptive scheme involving the following steps:

1. Defining the variation range  $\beta$  of  $h_i$  and the sampling interval  $\Delta h$
2. Determining the optimal  $h_i$  based on the normalization of the cumulative weight of neighboring points
3. Incorporating the best  $h_i$  into the improved weight function to complete the interpolation.

In this study,  $\beta$  is determined as  $[d_p, 6d_p]$  to make sure the enough support points of each interpolation point and avoid excess smoothing.  $\Delta h$  is set as  $0.5d_p$ .

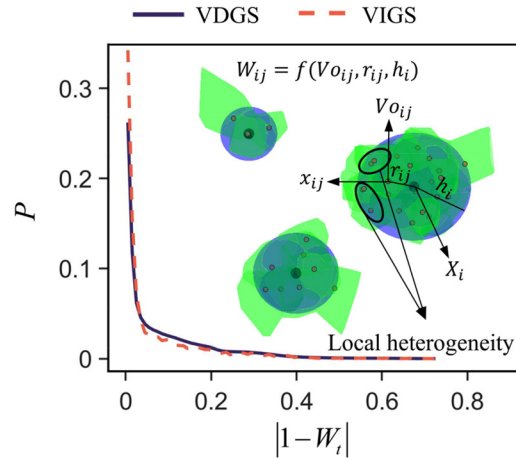


FIG. 4. The VWGI method and the normalization of the kernel function. The black point is interpolation point ( $X_i$ ), the red point is the surrounding points ( $x_{ij}$ ) of  $X_i$ , the blue sphere is the support zone of  $X_i$ , the green convex polyhedra is the Voronoi cell of  $x_{ij}$ , and  $Vo_{ij}$  represents its volume. The line graph is the probability density distribution of  $|1 - W_i|$ , and  $W_i$  is the cumulative weight of surrounding particles for each mesh point within 14–14.8 s. The bin width is 0.01.

To acquire continuous fields of particle dynamic features, we establish a uniform cubic mesh to discretize the cylinder, with a mesh size of  $0.8d_p$ . The VWGI method is employed to compute the corresponding values at each mesh point for each time snapshot. We adopt a sampling frequency of 400 Hz. The critical volume fraction is determined based on the time-averaged volume fraction of each mesh point. Mesh points with lower volume fractions are considered outside the system boundary. Finally, the continuous field is obtained by time-averaging the values of the mesh points within the system.

To assess the effectiveness of the VWGI method, we record the cumulative weight of surrounding particles ( $W_i$ ) for each mesh point within both systems over a fully developed period from 14 s to 14.8 s. The probability density distribution of  $|1 - W_i|$  is illustrated in Fig. 4. Notably,  $|1 - W_i|$  within both systems exhibit values below 0.2, affirming the VWGI method's ability to faithfully estimate continuous fields for both immersed and dry systems.

## III. RESULTS AND DISCUSSION

### A. Kinematics of discrete particles

#### 1. Temporal variation of particle kinematics

Our focus lies in the particle dynamics of the VIGS after reaching a fully developed stage. Hence, all statistical analyses in the paper were performed after 14 s. We initially investigate the temporal variation of the system kinetic energy ( $E_{TK}$ ) for both VDGS and VIGS, as illustrated in Fig. 5

$$E_{TK} = \sum E_K, \tag{17}$$

$$E_K = \frac{1}{2} m_p \|U_p\|^2, \tag{18}$$

where  $E_{TK}$  is the kinetic energy of one particle inside the system and  $U_p$  is the particle's velocity.

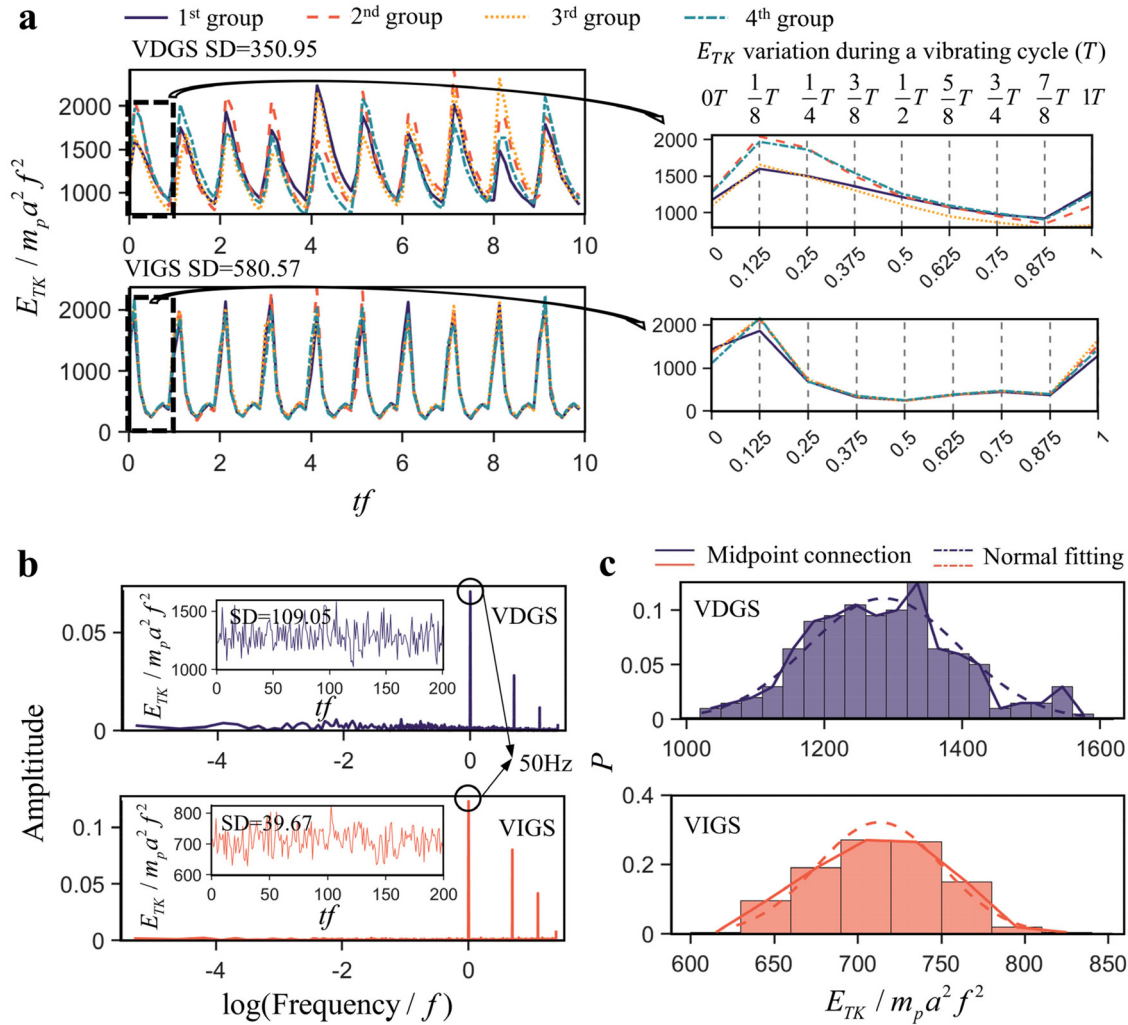


**FIG. 5.** Temporal variation of  $E_{TK}$ . SD refers to the data standard deviation. (a) Temporal variation of  $E_{TK}$  after fully developed. The  $E_{TK}$  values during four distinct time intervals (the first group (14.0–14.2 s); the second group (15.0–15.2 s); the third group (16.0–16.2 s); and the fourth group (17.0–17.2 s) are extracted. (b) Normalized amplitude of the  $E_{TK}$  temporal variation frequency. The subgraph shows the time-averaged  $E_{TK}$  of each vibrating cycle. (c) Probability density distribution of the time-averaged  $E_{TK}$  of each cycle. The duration for analysis is 200 vibrating cycles. The bin width is 30.

We extract values during four distinct time intervals: the first group (14.0–14.2 s), the second group (15.0–15.2 s), the third group (16.0–16.2 s), and the fourth group (17.0–17.2 s), as depicted in Fig. 5(a). Notably, after both systems reach fully developed,  $E_{TK}$  variations in both exhibit conspicuous periodicity, with a frequency matching the vibrating frequency (50 Hz). Then, we analyze the  $E_{TK}$  variation during a vibrating period ( $T$ ). From  $0T$  to  $T/8$ ,  $E_{TK}$  of both systems experience an increase followed by a decline during  $T/8$  to  $T/2$ . Subsequently,  $E_{TK}$  variation diverges between the VDGS and VIGS. In the VDGS,  $E_{TK}$  continues to decrease until  $7T/8$ , whereas in the VIGS,  $E_{TK}$  shows a slight rise during  $T/2$  to  $3T/4$  before decreasing. Notably, the degree of variation of  $E_{TK}$  within a cycle is more pronounced in the VIGS compared to the dry system. While the maximum kinetic energy in both systems is nearly identical, the corresponding minimum  $E_{TK}$  in the VIGS is significantly lower. This observation underscores the higher

energy dissipation efficiency in the immersed system compared to the dry system. Furthermore, the dry system displays more pronounced fluctuation of  $E_{TK}$  among different cycles.

We employed the Fourier transform to analyze the signal amplitude of the  $E_{TK}$  variation frequency, as presented in Fig. 5(b). Notably, Fig. 5(b) reveals that  $E_{TK}$  of both systems exhibit periodic vibrations that prominently peak at the forced vibration frequency of 50 Hz. Remarkably, the VIGS displays a higher normalized signal amplitude compared to the VDGS. To further quantify the fluctuations in  $E_{TK}$  among different cycles, we calculate the time-averaged  $E_{TK}$  for each cycle. The subgraph within Fig. 5(b) illustrates the standard deviation of these time-averaged  $E_{TK}$  values, revealing a more pronounced  $E_{TK}$  fluctuation among different cycles in the dry system. This observation indicates that the larger standard deviation of  $E_{TK}$  in the VIGS is primarily driven by the evident  $E_{TK}$  variation during each cycle.



In Fig. 5(c), we present the probability density distribution of the time-averaged  $E_{TK}$  values for each cycle. This distribution analysis indicates that both systems exhibit  $E_{TK}$  fluctuations among different cycles that conform to a normal-like distribution. Upon reaching fully development, the VDGS demonstrates time-averaged  $E_{TK}/m_p a^2 f^2$  values for each cycle fluctuating at a higher level, approximately 1290, whereas the corresponding value for the VIGS is approximately 710.

The analyses thus far have focused primarily on the temporal variation of system kinetic energy, without delving into the variations in different kinetic energy grades. The normal-like fluctuation of the time-averaged  $E_{TK}$  for each cycle demonstrates that particle kinetic energy ( $E_K$ ) at the same time point during a vibrating cycle can capture general characteristics of the different time points during a vibrating cycle, it is crucial to explore temporal variations in different kinetic energy grades among time point during a vibrating cycle. To address this, we have counted  $E_K$  and particle volume fraction ( $C$ ) at different time points during a vibrating cycle (specifically,  $0T$ ,  $T/8$ ,  $T/2$ ,  $3T/4$ ,  $7T/8$ ) within the time interval of 200 vibrating cycles. The selection of these time points is based on our previous analysis of  $E_{TK}$ . We have obtained the corresponding probability density distributions, as depicted in Fig. 6

$$C = \frac{V_p}{V_o}, \quad (19)$$

where  $V_p$  is the volume of the particle and  $V_o$  is the Voronoi cell volume of this particle.

Figures 6(a) and 6(b) reveal that, throughout the vibration cycle, the content of particles with low  $E_K$  remains stable, while the difference emerges at the content of particles with high  $E_K$ . As  $E_K$  increases, the variation of the content of particles with correspond  $E_K$  becomes more pronounced, with the immersed system exhibiting a greater degree compared to the dry system. In the VIGS, from  $0T$  to  $T/8$ , there is an increase in the content of particles with high  $E_K$ , followed by a decrease over time. By  $T/2$ , this content reaches its lowest point, with a slight increase afterward. Between  $3T/4$  and  $7T/8$ , there is another decrease in the content of high  $E_K$  particles. Conversely, in the VDGS, the content of particles with high  $E_K$  continues to decline until  $7T/8$  after an initial increase from  $0T$  to  $T/8$ , aligning with the pattern of  $E_{TK}$  variations during a vibrating cycle. This suggests that periodic changes in  $E_{TK}$  are primarily driven by fluctuations in the content of particles with high  $E_K$ . Figures 6(c) and 6(d) reveal that, in both systems, the content of particles with high  $C$  remains consistent throughout the vibration cycle, while the content of particles with low  $C$  exhibit significant variations, with the VIGS displaying a higher degree of variation.

Both immersed and dry systems experience notable changes in the content of particles with high  $E_K$  and low  $C$  during a cycle. This raises the question of whether these are the same particles and what their approximate spatial locations might be.

Given that the systems are subjected to vertical vibration, particle properties may vary with changes in height. Therefore, we introduce the particle height ( $H_p$ ) to determine the location of particles with conspicuous  $E_K$  and  $C$  temporal variations. Based on the maximum height

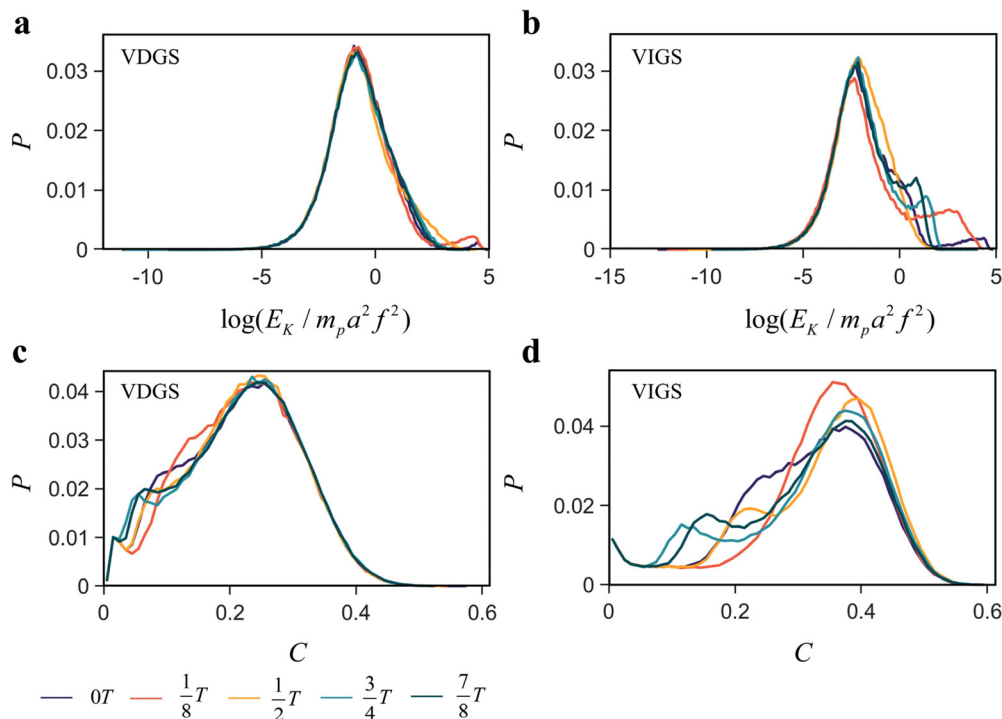


**FIG. 6.** Probability density distribution (PDF) of  $E_K$  and  $C$  at different time points during a vibration cycle. (a) PDF of  $E_K$  for dry case; (b) PDF of  $E_K$  for immersed case; (c) PDF of  $C$  for dry case; (d) PDF of  $C$  for immersed case. The time periods are selected as  $0T$ ,  $T/8$ ,  $T/2$ ,  $3T/4$ ,  $7T/8$ , respectively. The duration for analysis is 200 vibrating cycles. The bin widths of  $E_K$  and  $C$  are 0.1 and 0.01, respectively.

of the system, the VIGS has been segmented into three distinct height intervals:  $H_y \in [0, 5d_p]$ ,  $H_y \in (5d_p, 10d_p]$  and  $H_y \in (10d_p, 15d_p]$ . Due to the larger height range in the dry system, an additional interval  $H_y \in (15d_p, 20d_p]$  is introduced. To provide insights into the system behavior at different time points during a vibrating cycle, we have obtained and presented the probability density distributions of both  $E_K$  and  $C$  within these various height intervals, as illustrated in Fig. 7.

Observations from Figs. 7(a) and 7(b) indicate that when  $H_y$  exceeds  $5d_p$ , there is a noticeable absence of temporal changes in both  $E_K$  and  $C$  across both systems. Conversely, the temporal variations in  $E_K$  and  $C$  of heights below  $5d_p$  closely resemble the patterns observed in the global space. As  $H_y$  increases,  $E_K$  experiences a decline, with the rate of decrease diminishing. It can be seen from Figs. 7(c) and 7(d) that, as  $H_y$  increases,  $C$  initially increases before subsequently decreasing. Consequently, particles located at the bottom of the system tend to exhibit higher  $E_K$  and lower  $C$ , and these two features undergo more pronounced temporal variations compared to particles at higher elevations, contributing to the periodic fluctuations observed in  $E_{TK}$ .

Collisions play a fundamental role in the transfer of kinetic energy within granular systems, and they offer insights into the temporal variations observed in  $E_K$ . We counted particle collisions over 5 vibrating cycles. Figure 8 depicts the collision counts involving particle–wall interactions (where “wall” refers to the bottom vibrating wall) and particle–particle interactions ( $H_y \leq 5d_p$  and  $H_y > 5d_p$ ) for both systems. In Fig. 8(a), it is evident that the collision counts between particles and the wall exhibit periodic variations at the same frequency (50 Hz) and follow a consistent pattern in both systems. These counts increase to the peak values at  $T/8$  and then gradually decline until

$3T/8$ , after which they remain at zero. This trend indicates that particles in both systems entirely disengage from the vibrating wall after the  $3T/8$ . Figure 8(b) illustrates the periodic nature of collision count variations among particle–particle interactions ( $H_y \leq 5d_p$ ) in both systems, which is akin to that of the particle–wall interactions. Beyond a certain height ( $H_y > 5d_p$ ), the particle collision counts in both systems exhibit random fluctuations over time, devoid of periodicity.

To sum up, the vibrating wall imparts energy to and dislodges bottom particles through collisions, which makes these particles exhibit higher  $E_K$  and lower  $C$ . The periodic motion of the vibrating wall leads to periodic variations in the kinematical features of these “heated” particles. Kinetic energy is transmitted through these collisions and gradually dissipates, resulting in a decrease in  $E_K$  in the vertical direction. Particles situated at intermediate heights act as effective buffers, causing the temporal variations in  $E_K$  to deviate from the influence of the vibrating wall’s periodic motion. Lower particles possess longer particle free paths due to the looseness of the vibrating wall, resulting in fewer collisions, while upper particles experience numerous collisions owing to their shorter free paths. However, it’s important to note that collision counts may not fully encapsulate the energy dissipation process during collisions, as the initial velocity differences between colliding particles also play a crucial role.

2. Spatial distribution of particle kinematics

As the kinematical features of particles above  $5d_p$  remain stable without periodicity, the long-term statistic of them offers a reliable representation of the general particle kinematics within this height range.

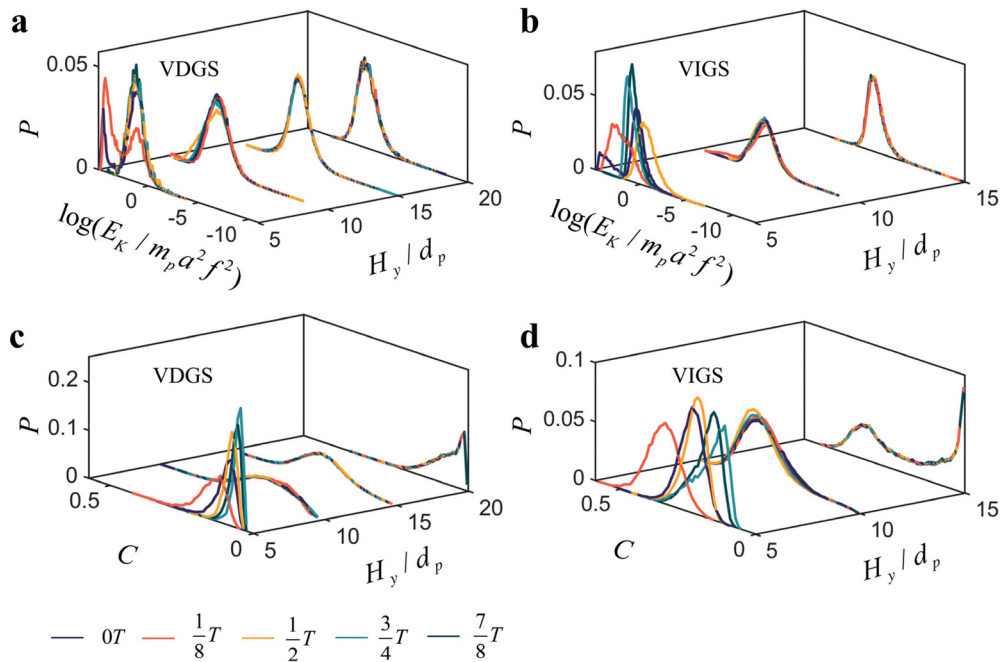
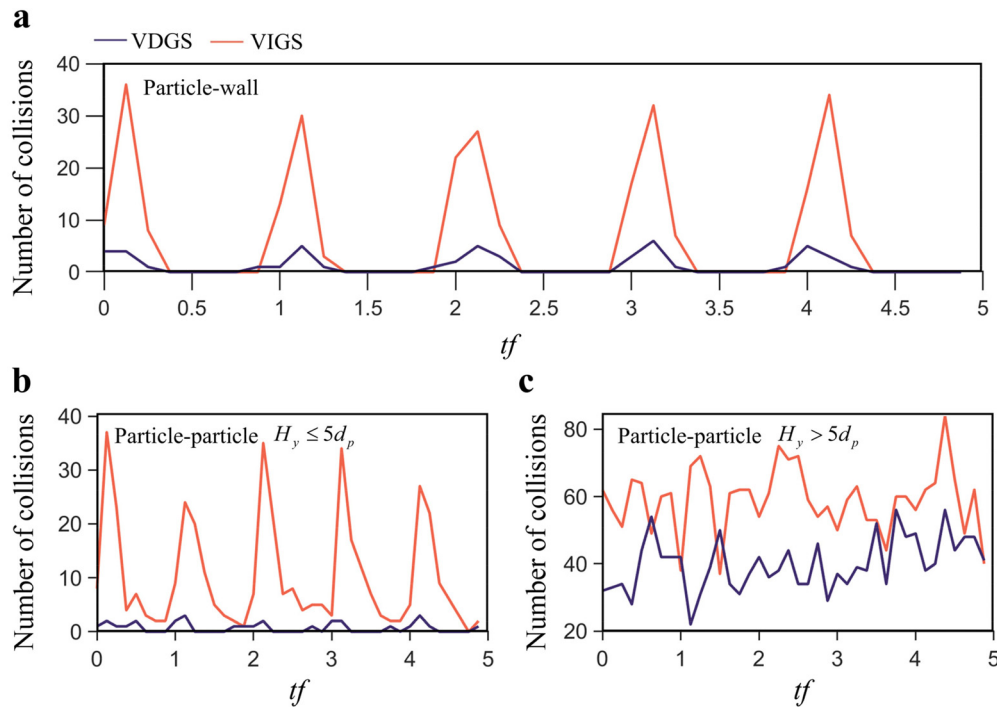


FIG. 7. Probability density distribution (PDF) of  $E_K$  and  $C$  in  $H_y$  intervals. (a) PDF of  $E_K$  for dry case; (b) PDF of  $E_K$  for immersed case; (c) PDF of  $C$  for dry case; (d) PDF of  $C$  for immersed case. The time periods are selected as  $0T$ ,  $T/8$ ,  $T/2$ ,  $3T/4$ ,  $7T/8$ , respectively.  $H_y$  is separated into three intervals in the VIGS ( $H_y \in [0, 5d_p]$ ,  $H_y \in (5d_p, 10d_p]$ ,  $H_y \in (10d_p, 15d_p]$ ). A higher interval ( $H_y \in (15d_p, 20d_p]$ ) is added in the VDGS. The distribution line of each  $H_y$  interval is drawn at the interval’s upper boundary. The duration for analysis is 200 vibrating cycles. The bin widths of  $E_K$  and  $C$  are 0.1 and 0.01, respectively.



**FIG. 8.** Collision counts temporal variation in the dry and immersed systems. The duration for analysis is five vibrating cycles. (a) Temporal variation of the particle–wall collision counts. (b) Temporal variation of the particle–particle ( $H_y \leq 5d_p$ ) collision counts. (c) Temporal variation of the particle–particle ( $H_y > 5d_p$ ) collision counts.

We have generated probability density distributions of the kinetic energy of particles ( $H_y > 5d_p$ ) in three dimensions ( $E_{xK}$ ,  $E_{yK}$ , and  $E_{zK}$ ), presenting in Fig. 9(a). It is evident from Fig. 9(a) that  $E_{yK}$  exceeds both  $E_{xK}$  and  $E_{zK}$  in both systems, while  $E_{xK}$  closely mirrors  $E_{zK}$ . In Sec. III A 1, we analyzed the distribution of  $E_K$  and  $C$  along the Y-direction. In this section, we delve into the spatial distribution of particle kinematical features in the X- and Z-direction, with the Y-direction particle information consolidated.

To describe the XZ location of each particle, we employ a polar coordinate system situated on the corresponding XZ plane, with its height set equal to  $H_y$ . The pole's Cartesian coordinates for each polar coordinate system are denoted as  $O(0, H_y, 0)$ . The polar axis originates from  $O$  and extends counterclockwise toward the positive direction of the X axis. The radial coordinate is designated as  $R_{xz}$ , and the angular coordinate as  $\theta \in [0, 2\pi)$ .  $\alpha_y \in [0, \pi]$  is defined as the angle between the particle velocity vector and the Y axis, where  $\alpha_y \in [0, 0.5\pi)$  represents motion toward the positive Y axis. The closer  $\alpha_y$  is to the 0 or  $\pi$ , the closer the moving direction is to the vertical. The denotation of  $\alpha_{xz} \in [0, 2\pi)$  is similar to  $\theta$ , which represents the counterclockwise rotating angle from the positive direction of the X axis to the projection of the particle velocity vector on the XZ plane, and  $\alpha_{xz} = 0$  indicates that the particle motion is horizontal to the positive direction of the X axis. The specific description is shown in Fig. 9(b).

The analysis of particle properties, specifically  $\alpha_y$ ,  $\alpha_{xz}$ ,  $E_K$ , and  $C$ , is conducted using angular and radial coordinates, as depicted in Figs. 10 and 11.

From Figs. 10(a) and 10(b), it is evident that  $\alpha_{xz}$  closely approximates  $\theta$  within the immersed system, and the dry system exhibits a

similar trend, albeit with a somewhat lower degree of correlation. Meanwhile, the probability density distribution of the other particle features remains relatively constant along  $\theta$ . In both systems, more particles move upward, while the moving direction of these particles is closer to vertical in the VIGS.

As depicted in Fig. 11,  $R_{xz}$  is divided into five intervals ( $R_{xz} \in [0, 1.4d_p]$ ,  $R_{xz} \in (1.4d_p, 2.8d_p]$ ,  $R_{xz} \in (2.8d_p, 4.2d_p]$ ,  $R_{xz} \in (4.2d_p, 5.6d_p]$ ,  $R_{xz} \in (5.6d_p, 7d_p]$ ), and the probability density distribution of  $\alpha_{xz}$  in both systems exhibits stability along  $R_{xz}$ . In contrast, the other three properties exhibit variations with changing  $R_{xz}$ , and this pattern is consistent across both systems. Specifically,  $E_K$  is highest near the cylinder's center and then gradually decreases as  $R_{xz}$  increases, with a more pronounced gradient observed in the immersed system. Conversely,  $C$  exhibits an opposing trend, increasing as  $R_{xz}$  increases, aside from the boundary region, signifying that lower  $E_K$  typically corresponds to higher particle concentration.

The probability density distribution of  $\alpha_y$  along  $R_{xz}$  also provides valuable insight into the velocity structure. In both systems, a significant percentage of particles near the cylinder's center move upward, while those near the sidewall predominantly move downward. This trend is more pronounced in the VIGS. When combined with the  $\alpha_{xz}$  variation along  $\theta$ , it suggests the formation of a velocity spatial structure of convection in both systems, moving from the cylinder's center toward the sidewall. Notably, in the VIGS, this convection exhibits greater uniformity along  $\theta$ , and velocity fluctuations in the  $\theta$  direction are considerably weaker compared to the dry system, indicating the potential to suppress the mixing process.

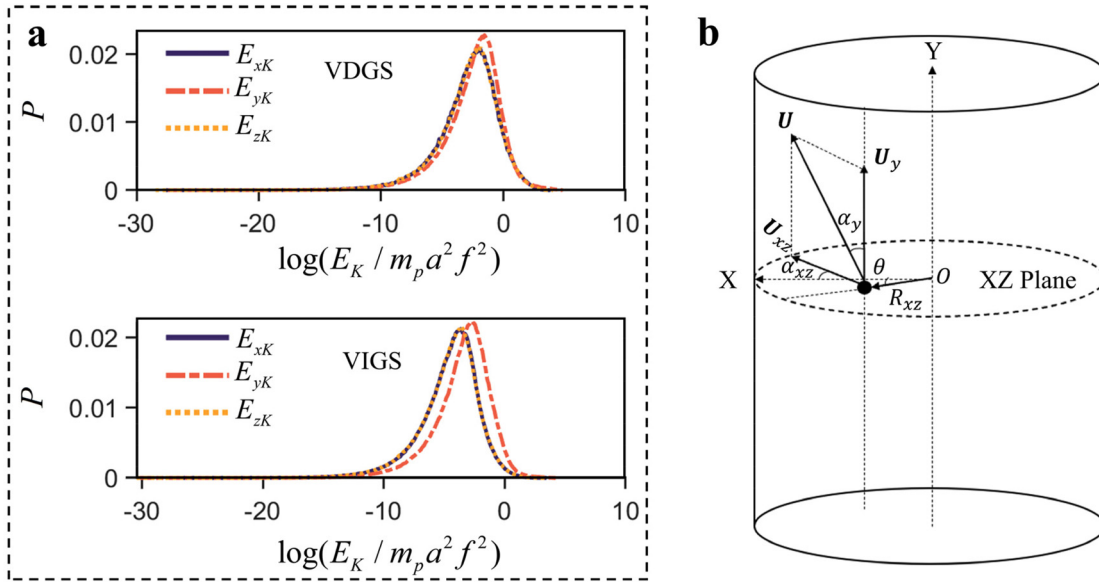


**FIG. 9.** Direction characteristics of particle kinematics. (a) Probability density distribution of  $E_{xK}$ ,  $E_{yK}$  and  $E_{zK}$  in the dry and immersed systems. The duration for analysis is 200 vibrating cycles.  $H_y > 5d_p$ . The bin width is 0.1. (b) Deposition method for the spatial distribution of the particle kinematics in the X- and Z-direction. The black point represents a particle.

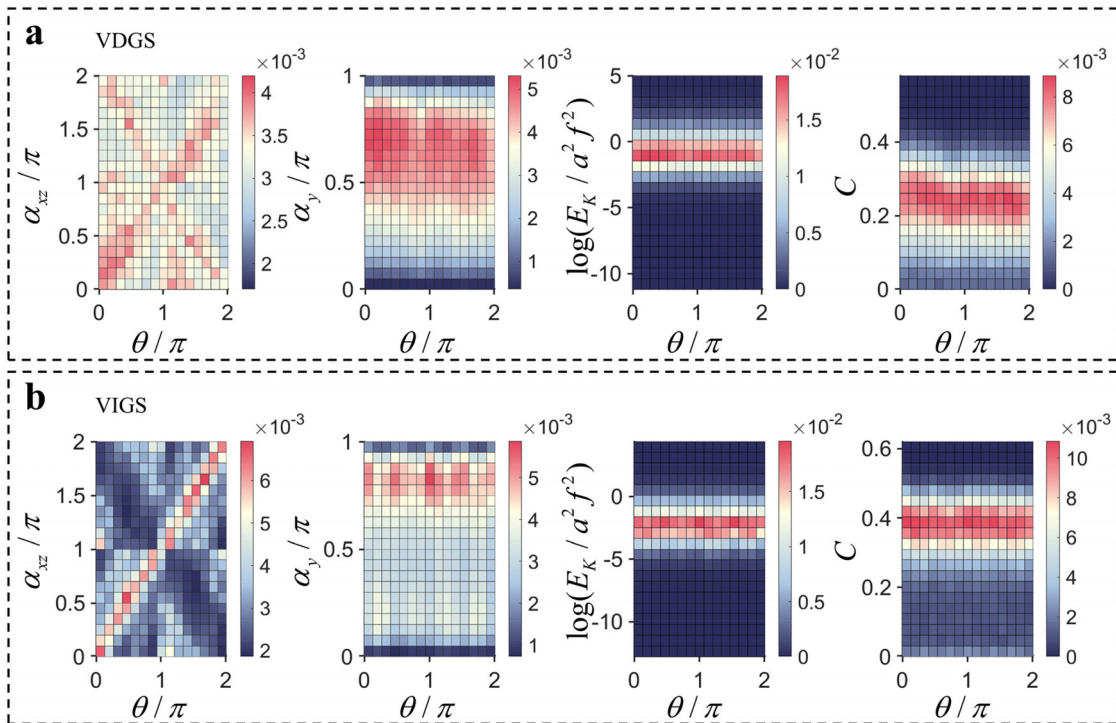


**FIG. 10.** Probability density distribution of  $\alpha_{xz}$ ,  $\alpha_y$ ,  $E_K$ , and  $C$  along  $\theta$  for the dry and immersed systems. (a) for the dry case; (b) for the immersed case. The duration for analysis is 200 vibrating cycles.  $H_y > 5d_p$ .

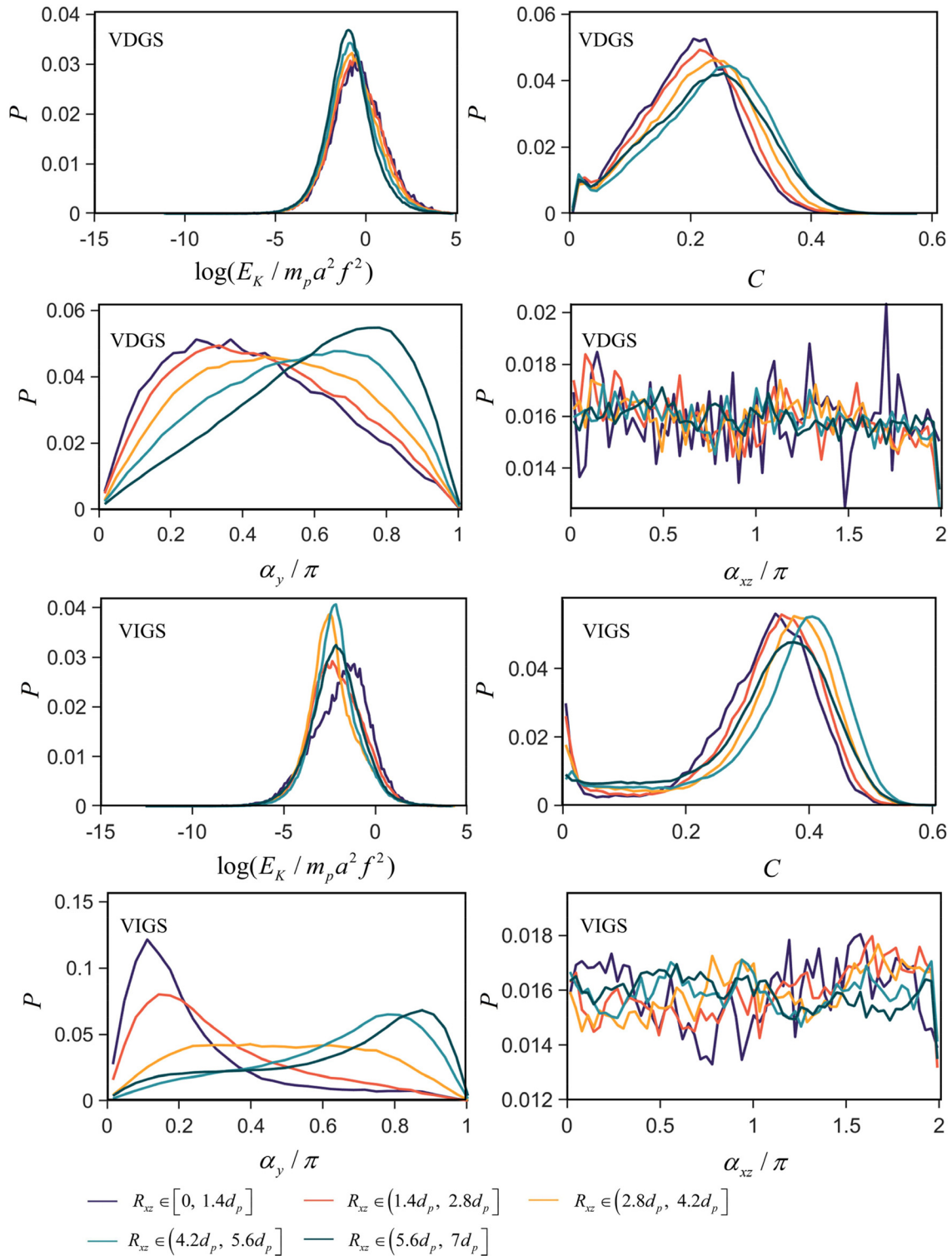


**FIG. 11.** Probability density distribution of  $E_K$ ,  $C$ ,  $\alpha_y$ , and  $\alpha_{xz}$  in  $R_{xz}$  intervals.  $H_y > 5d_p$ .  $R_{xz}$  of the two systems is separated into five intervals:  $R_{xz} \in [0, 1.4d_p]$ ,  $R_{xz} \in (1.4d_p, 2.8d_p]$ ,  $R_{xz} \in (2.8d_p, 4.2d_p]$ ,  $R_{xz} \in (4.2d_p, 5.6d_p]$ ,  $R_{xz} \in (5.6d_p, 7d_p]$ , respectively. The duration for analysis is 200 vibrating cycles. The bin widths are  $\alpha_y$  0.1,  $\alpha_{xz}$  0.1,  $E_K$  0.1, and  $C$  0.01, respectively.

08 April 2024 03:15:08

**B. Continuous analysis of particle dynamics**

**1. Local heterogeneity of particle distribution**

The system space has been discretized into uniform cubes, each with a size of  $2d_p$ . To assess the heterogeneity of particle distribution within local cells, we obtained the probability density distribution of  $C$  for each cube. Three cubes with the same  $H_y$  are selected for analysis, and the height levels are selected as 3 in the VIGS and 4 in the VDGS, as illustrated in Fig. 12.

As depicted in Fig. 12(a), the VIGS exhibits a high degree of local uniformity in particle distribution near the center of the cylinder, with  $C$  showing a normal-like distribution in the central cubes. However, this uniformity degrades as the increase in  $R_{xz}$ . On the other hand, Fig. 12(b) illustrates that although the VDGS displays consistent local heterogeneity in particle distribution across different spatial locations,  $C$  does not strictly adhere to a normal distribution. In both systems, as shown in Figs. 12(c) and 12(d), particle local heterogeneity is more concentrated and less pronounced in the dry system. Additionally, the gradient of  $C$  exists along  $H_y$  and  $R_{xz}$  in the two systems, indicating non-uniformity on a larger scale. Consequently, the utilization of the VWGI method is crucial for obtaining an accurate continuous field representation of particle dynamical features in both systems.

**2. Quantifying description of convection**

Velocity,  $E_K$ , and  $C$  fields of both systems have been successfully obtained by the VWGI, as illustrated in Fig. 13. The statistical duration is 40 vibrating cycles. These velocity fields reveal the presence of a velocity spatial structure of convection in both systems. Notably,  $\alpha_{xz}$  is

nearly identical to  $\theta$ . The spatial distribution of  $E_K$  and  $C$  closely aligns with the analyses in Sec. III A 2. Specifically, the  $E_K$  valley corresponds to the convection center. Large  $E_K$  regions are associated with convection, occurring diagonally below the convection center and near the cylinder's central axis. The location of the large  $C$  regions is also related to the convection, appearing diagonally up the convection center and near the sidewall. Furthermore, the convection center is positioned lower in the VIGS compared to the VDGS.

Quantitative characterization of the convection necessitates determining the convection center and calculating its strength. While the velocity field vector plot can provide an approximate convection center, it introduces subjectivity. Despite the convection center displaying low  $E_K$ , a larger region with a similar  $E_K$  grade is observed in the upper part of the VIGS's central region. The most discernible steering motion is concentrated at the convection center, which helps us to estimate its location. Since  $\alpha_{xz}$  is almost equivalent to  $\theta$  and other properties remain constant along  $\theta$ , the convection's longitudinal section at each  $\theta$  is uniform. Therefore, the XY plane ( $Z = 0$ ) is selected for convection center determination. Near the convection center, horizontal movement will exhibit a noticeable reversal along the Y axis, while vertical movement will experience an evident reversal along the X axis.

In Sec. III A 2,  $\alpha_y$  is defined, where  $\alpha_y \in [0, 0.5\pi)$  represents upward particle motion and  $\alpha_y \in (0.5\pi, \pi]$  represents downward motion. Thus, vertical movement reversal can be sensitively detected by  $\alpha_y$ , while horizontal steering can be captured by  $\alpha_x$  (representing horizontal particle movement). On the chosen plane,  $\partial\alpha_y/\partial X$  and  $\partial\alpha_x/\partial Y$  are calculated to locate the convection centers, as depicted in Fig. 14. It is evident from Fig. 14 that the convection centers of both systems have been accurately identified using  $\partial\alpha_y/\partial X$  and  $\partial\alpha_x/\partial Y$ .

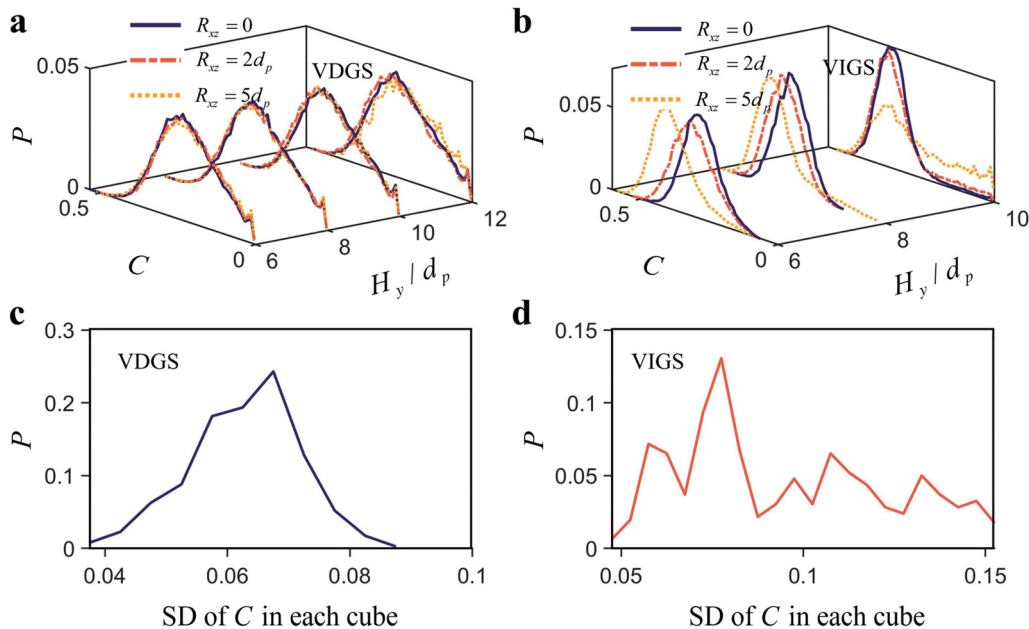


**FIG. 12.** Local heterogeneity of particle distribution in the dry and immersed systems. The duration for analysis is 200 vibrating cycles. (a) and (b) Probability density distributions of  $C$  in the sampled cubes for dry and immersed cases, respectively. Three cubes at the same  $H_y$  are sampled ( $R_{xz} = 0, R_{xz} = 2d_p, R_{xz} = 5d_p$ ), and the sampled heights are  $H_y = 6d_p, H_y = 8d_p, H_y = 10d_p, H_y = 12d_p$  in the VDGS and  $H_y = 6d_p, H_y = 8d_p, H_y = 10d_p$  in the VIGS, respectively. The bin width is 0.01. (c) and (d) Probability density distribution of the standard deviation of  $C$  in each cube for dry and immersed cases, respectively. The bin width is 0.01.

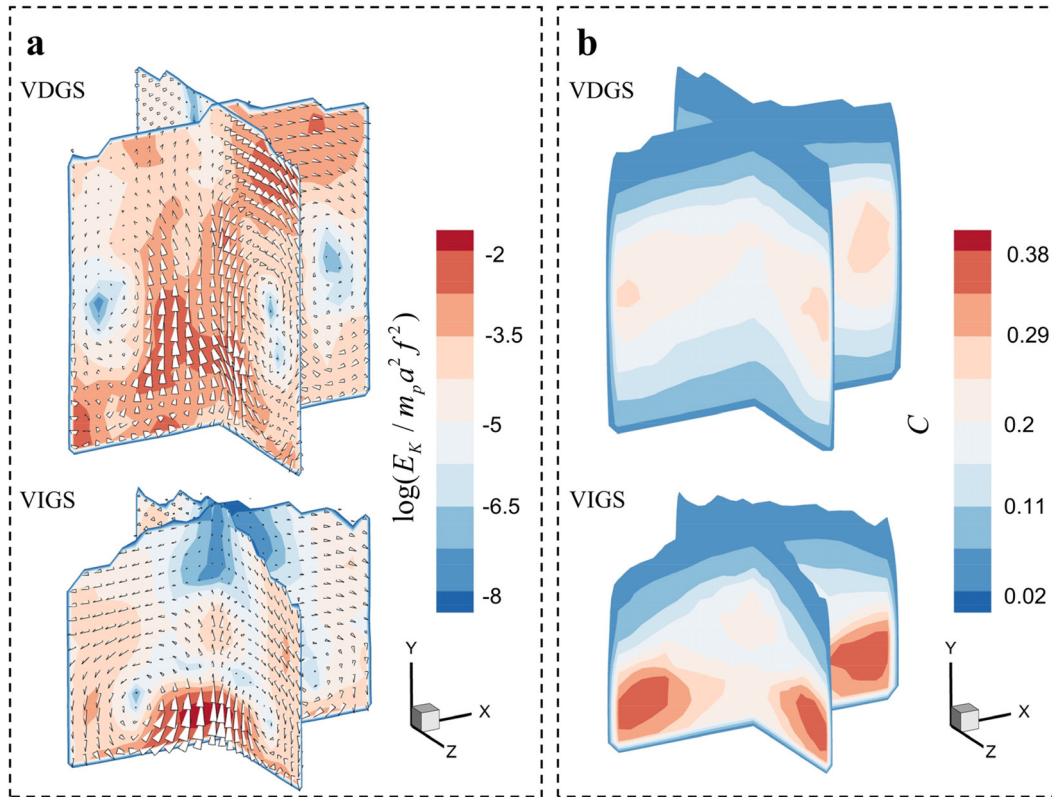


**FIG. 13.** Time-averaged continuous field of  $E_K$ ,  $C$  and the velocity vectors obtained by the VWGI method. (a) for  $E_K$  and (b) for  $C$ , respectively. The duration for analysis is 40 vibrating cycles. XY plane ( $Z = 0, Y > 5d_p$ ) and YZ plane ( $X = 0, Y > 5d_p$ ) are shown.

Despite a larger capturing range for the convective center in the VDGS, the central region aligns with the judgment from the velocity vector plot. The convection centers are located at about  $H_y = 7d_p, R_{xz} = 3.8d_p$  in the VIGS and  $H_y = 11.5d_p, R_{xz} = 5d_p$  in the VDGS, respectively.

The angular velocity  $A$  of the convection is introduced to reflect the convection strength, as expressed in the following equation:<sup>74</sup>

$$A = \frac{\sum_{i=1}^N \frac{\|\mathbf{U}_i\| \sin \alpha_i}{\|\boldsymbol{\lambda}_i\|}}{N}, \quad (20)$$

where  $N$  is the point number consisted in the convection roll,  $\|\mathbf{U}_i\|$  is the velocity magnitude of the  $i$ th point,  $\|\boldsymbol{\lambda}_i\|$  is the modulus of the vector from the convective center to the  $i$ th point, and  $\sin \alpha_i$  represents the counterclockwise rotation angle from  $\boldsymbol{\lambda}_i$  to  $\mathbf{U}_i$ . The specific description is shown in Fig. 14(b).

Based on the definition of  $\sin \alpha_i$ ,  $A < 0$  represents a clockwise rotation convection,  $A > 0$  represents a counterclockwise rotation. There is a positive correlation between  $|A|$  and the convection strength. It can be seen from Fig. 14 that, in the two systems, the angular velocity magnitude of the right convection ( $|A_r|$ ) is almost the same as the  $|A_l|$ , which indeed demonstrates that the convection features are uniform along  $\theta$ . Convection strength is stronger in the VIGS compared to the VDGS, which is mainly because of that the velocity

directionality of the discrete particles within the VDGS is worse, resulting in smaller  $\|\mathbf{U}_i\|$  after continuous treatment. As we all know, the convection strength reflects the macroscopic fluidity, thereby the kinetic energy of discrete particles is not positively correlated with their macroscopic fluidity. The gas-like particle motion found in the dry system may also have a convective velocity structure, while its macroscopic fluidity may not be stronger than the immersed system (particles moving like fluid). As for VDGS, with the increase in the kinetic energy of discrete particles, the  $|A|$  peak may be found, which will be further studied in our future work.

The convection in VDGSs has already been investigated using natural convection theory.<sup>25,30</sup> In our study, the convection in the VIGS is also similar to natural convection, which prompts the inquiry as to whether, under suitable conditions, it is conceivable to discern natural convection exhibiting velocity structure akin to the convection in both immersed and dry particle systems.

### 3. Analog of the convection in VGs to natural convection

At the microscopic level, molecules and atoms in fluid are in constant motion, exhibiting rapid vibrational, rotational, and collisional movements. These microscopic thermal motions determine the macroscopic properties of the fluid, including its temperature. Enhanced thermal motion of the microscopic particles corresponds to an increase

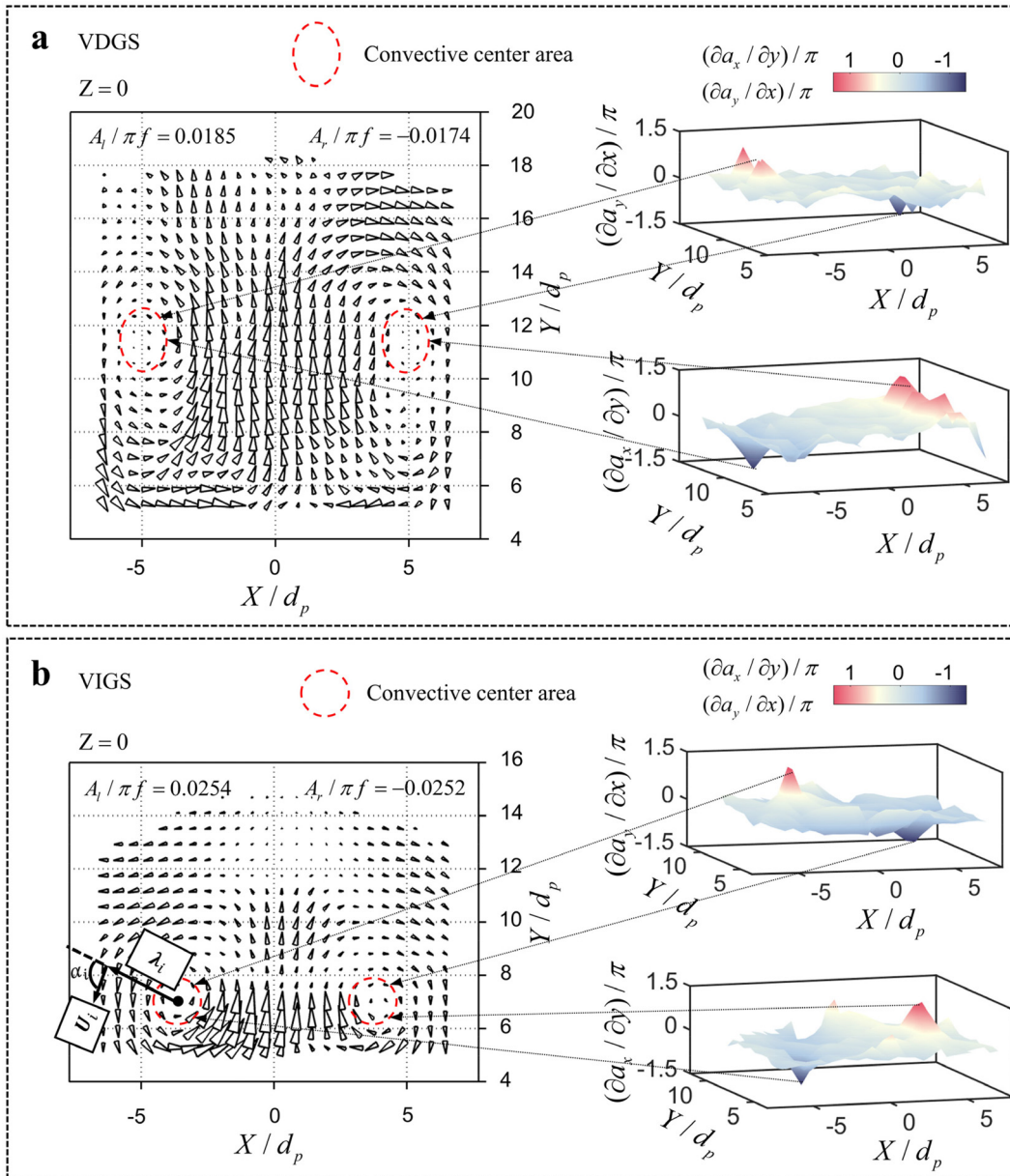


**FIG. 14.** Convection center and angular velocity for the dry and immersed systems. (a) is the dry case and (b) is the immersed case. Velocity field data on the XY plane ( $Z = 0, Y > 5d_p$ ) are utilized in the calculations. The duration for analysis is 40 vibrating cycles.

in the fluid’s temperature. As for the vibration-driven particle systems studied in this paper, particles in close proximity to the vibrating wall exhibit more pronounced motion, analogous to the enhanced thermal motion of microscopic particles within the fluid, as if the macroscopic particles are “heated” by the vibrating wall. Heating the bottom wall of a closed cylindrical container filled with fluid results in the formation of natural convection. Considering the “heating” effect experienced by macroscopic particles due to the vibrating wall, it is reasonable to anticipate a notable resemblance in the velocity spatial structure of particle convection to that of natural convection.

In the same cylindrical container as two particle systems, natural convections with similar velocity structures to the particle convection have been observed. This investigation is performed by CFD simulation, employing the Boussinesq approximation to account for fluid density variations with temperature.<sup>75</sup> Natural convections corresponding to the VDGS and VIGS are computed with Rayleigh numbers ( $Ra$ ) are  $2.9 \times 10^4$  and  $4.8 \times 10^3$ , respectively. The specific simulation settings are outlined in Table II.

The velocity vector and convection center of the natural convections are shown in Fig. 15.



TABLE II. Parameters setting of the simulation of natural convection.

Parameters	Natural convection (Ra = 2.9 × 10 <sup>4</sup> )	Natural convection (Ra = 4.8 × 10 <sup>3</sup> )
Thermal expansion coefficient (K <sup>-1</sup> )	3.1 × 10 <sup>-4</sup>	2.1 × 10 <sup>-4</sup>
Dynamic viscosity (N s/m <sup>2</sup> )	5	20
Density (kg/m <sup>3</sup> )		995.3
Temperature of upper wall (K)		303.15
Temperature of bottom wall (K)		305.15
Temperature of sidewall (K)		303.15
Thermal diffusivity (m <sup>2</sup> /s)		1.43 × 10 <sup>-7</sup>

As depicted in Fig. 15, the corresponding natural convections have similar velocity spatial structures compared to that of both particle systems. As for the natural convection corresponding to the VDGS, the height of its convection center is about 9.5d<sub>p</sub> from the bottom heated wall. In the particle systems, the averaging height of the vibrating wall is 2d<sub>p</sub>, and thus, the relative height of the convection center from the vibrating wall in the VDGS is 9.5d<sub>p</sub>, which matches that of the corresponding natural convection. The radial locations of the convection centers of the VDGS and corresponding natural convection are R<sub>xz</sub> = 5d<sub>p</sub> and R<sub>xz</sub> = 4d<sub>p</sub>, respectively. The convection centers of the VIGS and corresponding natural convection are located at about H<sub>y</sub><sup>\*</sup> = 5d<sub>p</sub>, R<sub>xz</sub> = 3.8d<sub>p</sub> and H<sub>y</sub><sup>\*</sup> = 5d<sub>p</sub>, R<sub>xz</sub> = 4d<sub>p</sub>, respectively. H<sub>y</sub><sup>\*</sup> represents the relative height from the vibrating/heating wall.

In conclusion, under certain vibration condition, macroscopic particles can exhibit motion like natural convection. Although the detailed formula is not clear yet, this observation suggests a profound intrinsic connection between particle convection and natural convection, thereby opening up novel avenues for the development of particle convection theories and providing robust support for such endeavors.

4. Momentum transfer and diffusion

Quantifying momentum transfer and diffusion within particle systems is of paramount importance in understanding natural phenomena and chemical processes. The momentum transfer p<sub>c</sub> and momentum diffusion p<sub>d</sub> per unit volume (1 m<sup>3</sup>) in the two systems can be calculated as follows:

$$p_c^i = \frac{\left| \sum_{j=1}^K \mathbf{u}_j^i C_j^i \rho_p \right|}{K}, \tag{21}$$

$$p_c = \frac{\sum_{i=1}^N p_c^i}{N}, \tag{22}$$

$$p_d^i = \frac{\left| \sum_{j=1}^K \mathbf{u}_j^i C_j^i \rho_p - \frac{\sum_{k=1}^K \mathbf{u}_k^i C_k^i \rho_p}{K} \right|}{K}, \tag{23}$$

$$p_d = \frac{\sum_{i=1}^N p_d^i}{N}, \tag{24}$$

where K is the number of the time snapshot and p<sub>c</sub><sup>i</sup> and p<sub>d</sub><sup>i</sup> represent the momentum transfer and diffusion of the i<sup>th</sup> point.

p<sub>c</sub> and p<sub>d</sub> in the three dimensions and p<sub>c</sub><sup>i</sup> and p<sub>d</sub><sup>i</sup> in the Y-direction (p<sub>yc</sub><sup>i</sup> and p<sub>yd</sub><sup>i</sup>) are shown in Fig. 16.

As depicted in Fig. 16(a), it is evident that the other two dimensions' p<sub>c</sub> in both systems are notably lower compared to the Y-direction. This discrepancy can be attributed to the higher velocity magnitudes in the Y-direction resulting from vertical vibration. In particular, the Y-direction momentum transfer p<sub>c</sub> in the immersed system surpasses that in the dry system. The p<sub>yc</sub><sup>i</sup> peak primarily concentrates on the two sides of the convection center, with the side nearer to the cylinder center exhibiting a higher value. Notably, a larger p<sub>yc</sub><sup>i</sup> peak is

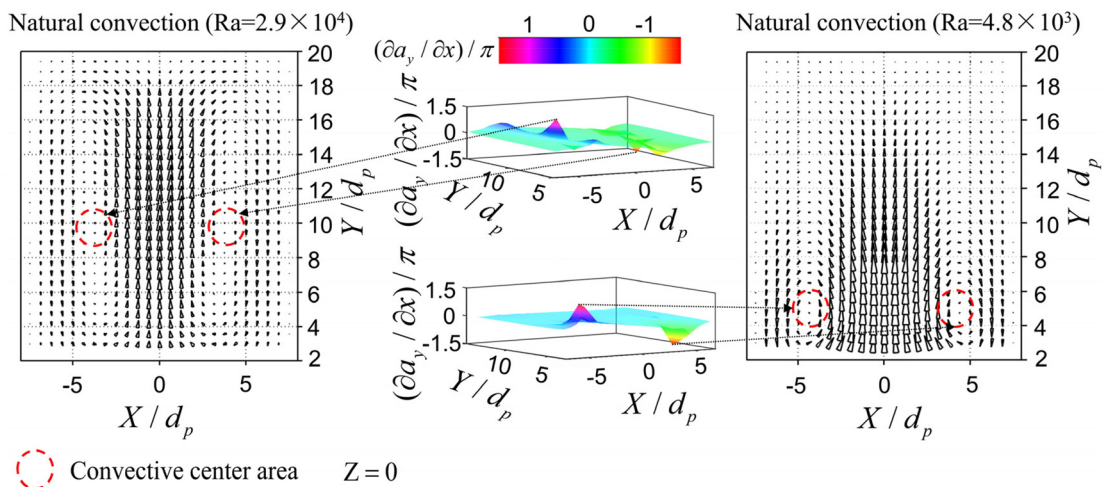
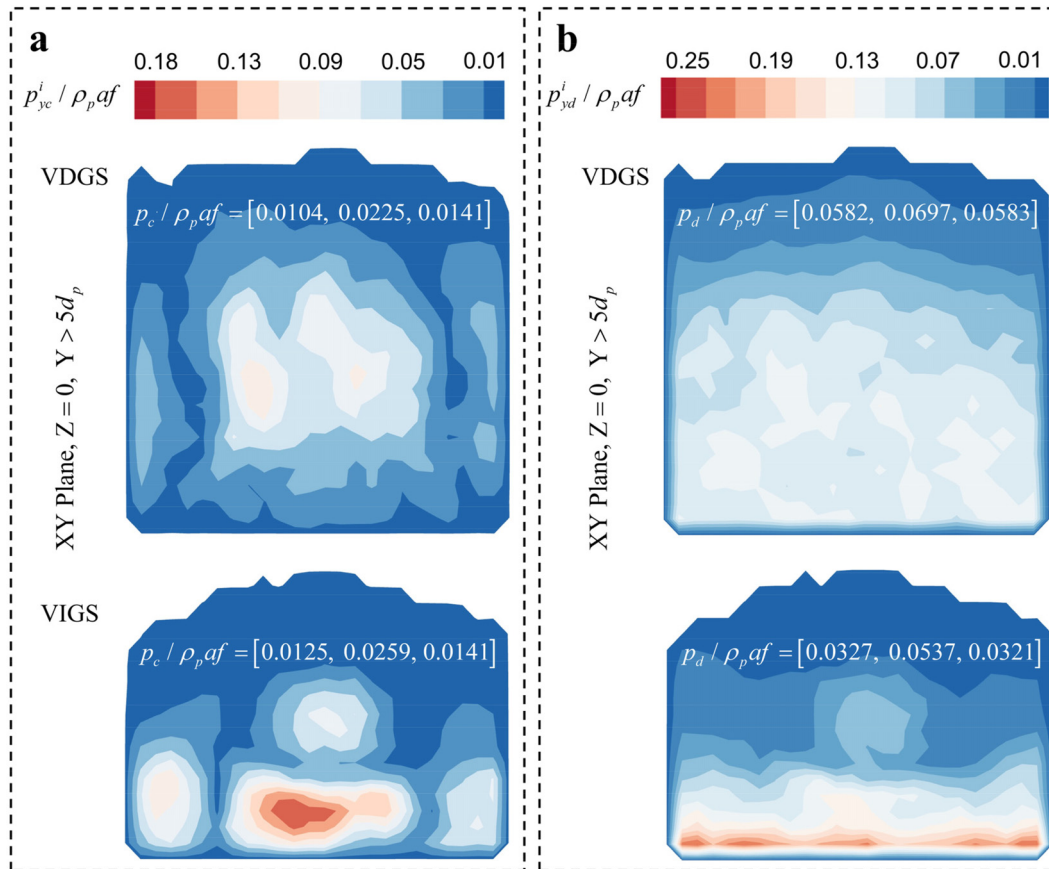


FIG. 15. Velocity vector and convection center of the natural convections when Rayleigh numbers are 2.9 × 10<sup>4</sup> and 4.8 × 10<sup>3</sup>, respectively. Velocity field data on the XY plane (Z = 0) are utilized in the calculations.



**FIG. 16.**  $p_{yc}^i$  and  $p_{yd}^i$  fields for the dry and immersed systems. (a) for momentum transfer  $p_c$  and (b) for momentum diffusion  $p_d$ . Field data of the velocity and  $C$  on the XY plane ( $Z = 0, Y > 5d_p$ ) is utilized in the calculation. The duration for analysis is 40 vibrating cycles.

observed in the VIGS, suggesting a positive correlation between convection strength and momentum transfer. This enhancement in convective motion facilitates the exchange of energy between “hot” and “cold” particles. Figure 16(b) reveals that  $p_d$  in the Y-direction also exceeds that in the other dimensions for both immersed and dry systems. However,  $p_d$  in the Y-direction is lower in the immersed system compared to the dry system. Furthermore,  $p_{yd}^i$  exhibits a distinct spatial distribution compared to  $p_{yc}^i$ , forming a relatively pronounced negative gradient along the Y-direction, with a more apparent gradient observed in the VIGS.

### C. Fluid effects on the particle movement

The field of the power of the fluid force acted on particles is also obtained by the VWGI method, and the power of the total fluid force ( $Power_t$ ), fluid drag force ( $Power_d$ ), and fluid buoyancy ( $Power_b$ ) are shown as the nephograms in Fig. 17(a). The probability density distribution of the discrete power of the fluid force is shown as the midpoint connections in Fig. 17(a).

The observations from Fig. 17(a) reveal that in the immersed system, the fluid force experienced by the particles is primarily dominated by the drag force, with the distribution of  $Power_d$  closely mirroring that of  $Power_t$ . Specifically, as one moves closer to the bottom,

the magnitude of  $Power_t$  and  $Power_d$  increases. The fluid force in the central region mainly performs negative work. Due to the presence of buoyancy and the upward particle velocity in the bottom central region, the negative region of  $Power_t$  is slightly smaller than that of  $Power_d$ . The negative  $Power_d$  illustrates that the fluid has a smaller or contrary velocity compared to the particles. With the height rising,  $Power_t$  declines gradually, demonstrating that the negative work of the fluid slows down the upward particles, and the velocity of these particles gradually approaches the fluid. However, the positive  $Power_d$  appears at a higher central region, illustrating that the upward fluid velocity exceeds the particle velocity. The small  $Power_d$  in this region also indicates that the velocity difference between the fluid and particles is not evident. Due to the existence of the buoyancy, the positive region of  $Power_t$  is slightly larger than that of  $Power_d$ .

At the same height near the sidewall,  $Power_t$ ,  $Power_d$ , and  $Power_b$  are all negative. The downward motion of the particles in this region indicates that the fluid moves downward with a lower velocity compared to the particles or moves upward with a small velocity. With the height reduction, the particles’ downward velocity gradually increases,  $Power_d$  is transformed from negative to positive, and then the positive value keeps increasing, which illustrates that the fluid’s downward

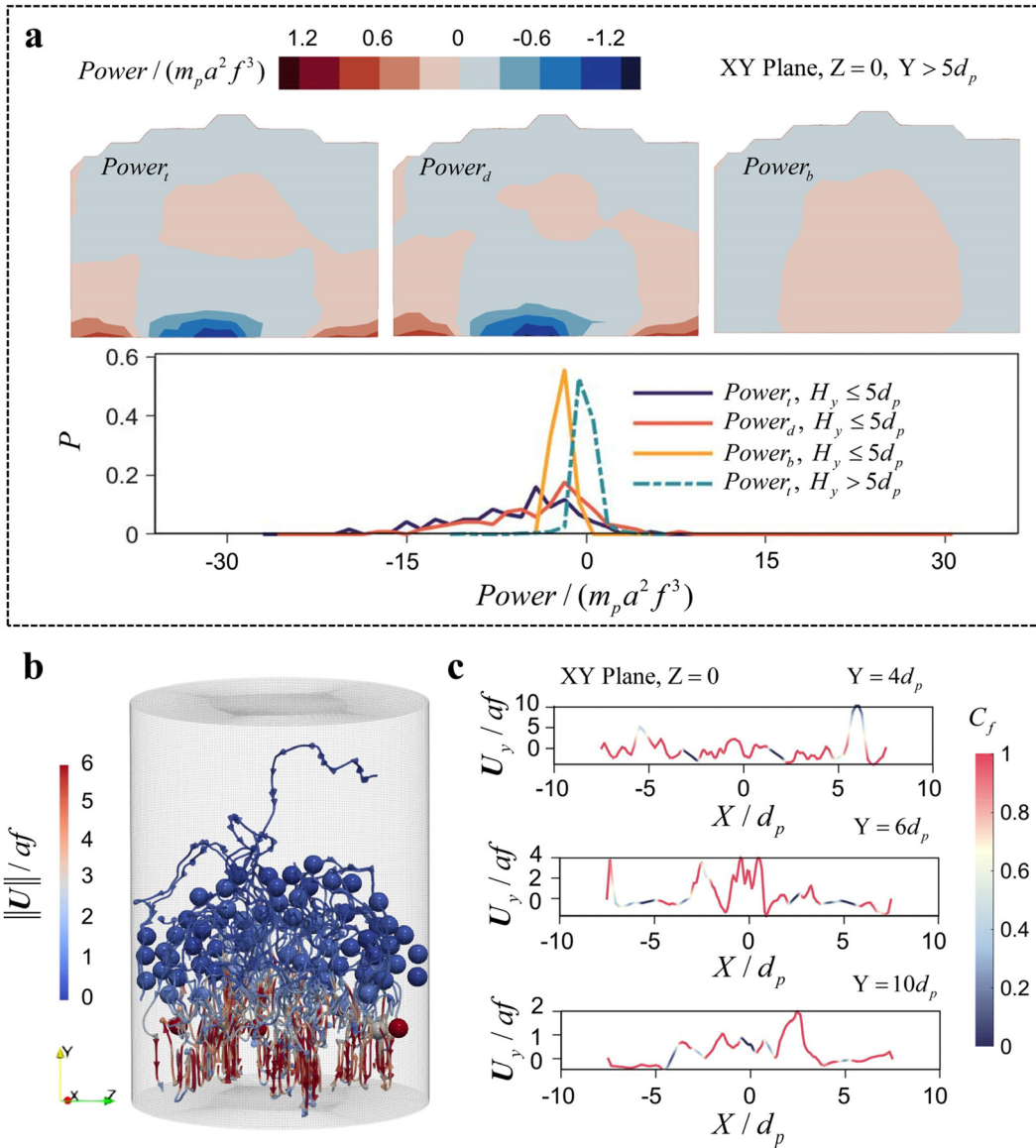


**FIG. 17.** Discussion of the fluid effects on the particle movement. (a) Continuous field and probability density distribution of the power of the fluid force on particles. The XY plane ( $Z = 0, Y > 5d_p$ ) is shown. The duration for analysis is 40 vibrating cycles. The bin width is 0.01. (b) Fluid velocity streamlines and particle velocity magnitude at 14 s. (c) Y-direction velocity on the characteristic lines at 14 s. The characteristic lines are located at the XY plane ( $Z = 0$ ), and their heights are  $4d_p, 6d_p,$  and  $10d_p$ , respectively.  $C_f$  is denoted as the volume fraction of fluid, and  $C_f < 0.3$  means the particles phase.

velocity also increases in this process, and the rising gradient is bigger than that of particles.

It can be seen from the midpoint connections in Fig. 17(a) that in the region above  $5d_p$ , the probability ratios of the positive and negative  $Power_t$  are basically consistent, which matches the continuous power field. However, under  $5d_p$ , a large number of particles are subjected to the negative fluid work, and  $Power_t$  magnitude is apparently larger than that above  $5d_p$ . Under  $5d_p$ , the content of the negative  $Power_d$  is larger than the positive power, and the distribution of  $Power_d$  and  $Power_t$  demonstrates that the drag force also performs the primary function in

this region. The content of the negative  $Power_b$  is also larger than the positive power, which illustrates that a large number of particles move downward under  $5d_p$ . However, the positive  $Power_b$  magnitude is obviously higher than that of the negative  $Power_b$ . Therefore, the particles under  $5d_p$  can be separated into two parts: most particles move downward with low velocity magnitude and prepare to be “heated” by the vibration particle wall, and other small portion of particles have been “heated” and move upward with high velocity magnitude.

The fluid streamlines in Fig. 17(b) demonstrate that a velocity spatial structure of convection is also formed in the fluid. At the upper

region, the lower power of the fluid force is caused by the basically consistent velocity of the fluid and particles. Three characteristic lines are selected on the XY plane ( $Z=0$ ), and the comprehensive velocity of the fluid and particles are recorded, as shown in Fig. 17(c). The fluid volume fraction  $C_f$  represents the fluid volume fraction, and  $C_f < 0.3$  means the particles phase. It can be seen from Fig. 17(c) that the convection structure of the fluid is not found under  $5d_p$ . In contrast, it is obvious upper  $5d_p$ , and the feature is similar to the particle convection in that the velocity is upward at the center and downward near the sidewall. Furthermore, the velocity difference between the fluid and particles decreases as the height increases, and the difference at  $4d_p$  is significantly greater than the higher characteristic lines.

In conclusion, in the lower region, the presence of the fluid not only hinders the energy acquisition of the downward moving particles but also enhances the energy dissipation of the particles after being “heated,” which might be the main reason for the VIGS stabilizing at a lower  $E_{TK}$  and showing a higher kinetic energy dissipation efficiency. However, in the upper region, the convection formation of the fluid, to some extent, is beneficial for the particle convection directionality.

#### IV. CONCLUSIVE REMARKS

The resolved CFD-DEM is introduced to simulate particle dynamics in the vibration-driven immersed granular system (VIGS) that is set in a hermetic cylinder container with a vertically vibrating wall at the bottom. The Voronoi-weighted Gaussian interpolation (VWGI) method is applied to convert the discrete particle information into a continuous field. The temporal variation and spatial distribution of the kinematics of discrete particles are analyzed; the continuous analyses of particle dynamics (convection and momentum transfer) are performed. The conclusive remarks are listed as follows:

1. The VWGI method enables the faithful estimation of the continuous field for both immersed and dry systems, especially for those with large-scale non-uniformity and the heterogeneity particle distribution in local cells.
2. The periodic variation of the system kinetic energy ( $E_{TK}$ ) peaks at the forced frequency (50Hz), and the collision between the vibrating wall and the lower particles ( $H_y < 5d_p$ ) dominates this process. However, the immersed system distinguishes itself from the dry situation as it needs a shorter time to reach the equilibrium and then stabilizes at a lower  $E_{TK}$ . The VIGS shows a higher kinetic energy dissipation efficiency.
3. A velocity spatial structure of convection, moving from the cylinder center to the sidewall, is observed in both immersed and dry systems away from the bottom. And the kinetic energy ( $E_K$ ) and particle volume fraction ( $C$ ) patterns for both systems are also similar. Compared with the dry system, the VIGS has larger  $E_K$  and  $C$  variation gradients along the vertical and radial directions. It is worth noting that the convection in the VIGS possesses a stronger uniformity along the radial angle ( $\theta$ ), and the velocity fluctuation in the  $\theta$  direction is significantly weaker than in the dry system, providing a potential approach to restrain the mixing process.
4. In both immersed and dry systems, the Y-direction is the main direction for the momentum transfer  $p_c$  and momentum diffusion  $p_d$ . The momentum transfer peak is located at the two sides of the convection center. Compared with the dry system, a stronger convection is formed in the VIGS, and the convection center

is located at a lower height. The VIGS has larger  $p_c$  and smaller  $p_d$  in the Y-direction, demonstrating the convection strength has a positive correlation to the momentum transfer.

5. The particles in both immersed and dry systems have similar velocity spatial structures compared to the natural convections when Rayleigh numbers are  $2.9 \times 10^4$  and  $4.8 \times 10^3$ , respectively, which suggests a profound intrinsic connection between particle convection and natural convection.
6. On the one hand, the presence of the fluid hinders the energy acquisition of the downward moving particles and enhances the energy loss of the particles after being “heated,” which might be the main reason for the immersed system stabilizing at a lower  $E_{TK}$  and showing a higher kinetic energy dissipation efficiency compared to the dry system. On the other hand, the convection formation of the fluid benefits the particle convection directionality.

#### ACKNOWLEDGMENTS

This work was supported by the National Natural Science Foundation of China (Grant Nos. 12032005 and 12372386).

#### AUTHOR DECLARATIONS

##### Conflict of Interest

The authors have no conflicts to disclose.

#### Author Contributions

**Chi Wang:** Data curation (lead); Formal analysis (lead); Investigation (equal); Methodology (equal); Visualization (lead); Writing – original draft (lead). **Lubin Wei:** Project administration (supporting); Resources (supporting); Supervision (equal); Writing – review & editing (supporting). **Yi An:** Conceptualization (lead); Funding acquisition (lead); Investigation (equal); Methodology (equal); Project administration (lead); Resources (lead); Supervision (equal); Writing – review & editing (lead).

#### DATA AVAILABILITY

The data that support the findings of this study are available from the corresponding author upon reasonable request.

#### REFERENCES

- <sup>1</sup>H. An, C. Ouyang, F. Wang, Q. Xu, D. Wang, W. Yang, and T. Fan, “Comprehensive analysis and numerical simulation of a large debris flow in the Meilong catchment, China,” *Eng. Geol.* **298**, 106546 (2022).
- <sup>2</sup>M. Bilal, A. Xing, Y. Zhuang, Y. Zhang, K. Jin, Y. Zhu, and Y. Leng, “Coupled 3D numerical model for a landslide-induced impulse water wave: A case study of the Fuquan landslide,” *Eng. Geol.* **290**, 106209 (2021).
- <sup>3</sup>N. Pirhadi, J. Hu, Y. Fang, I. Jairo, X. Wan, and J. Lu, “Seismic gravelly soil liquefaction assessment based on dynamic penetration test using expanded case history dataset,” *Bull. Eng. Geol. Environ.* **80**(10), 8159–8170 (2021).
- <sup>4</sup>O. J. I. Kramer, J. T. Padding, W. H. van Vugt, P. J. de Moel, E. T. Baars, E. S. Boek, and J. P. van der Hoek, “Improvement of voidage prediction in liquid-solid fluidized beds by inclusion of the Froude number in effective drag relations,” *Int. J. Multiphase Flow* **127**, 103261 (2020).
- <sup>5</sup>B. Caudle, V. D. Brandão, M. B. Gorenssek, and C.-C. Chen, “Process model-based validation of the intensification of biomass fast pyrolysis in a fluidized bed via autothermal operation,” *ACS Sustainable Chem. Eng.* **10**(48), 15926–15938 (2022).

- <sup>6</sup>L. Feng, S. Wang, R. Zhang, Z. Chai, L. Ji, and M. Zeng, "Study on key factors affecting separation performance of aerated fluidized bed," *Int. J. Coal Prep. Util.* **42**(2), 171–190 (2022).
- <sup>7</sup>J. Liu, L. Wei, X. Zhu, and S. Wang, "Study on matching effect of operating variables and particle motion behavior in teeter bed separator," *Int. J. Coal Prep. Util.* **42**(7), 2156–2171 (2022).
- <sup>8</sup>C. Coste, "Shearing of a confined granular layer: Tangential stress and dilatancy," *Phys. Rev. E* **70**(5), 051302 (2004).
- <sup>9</sup>S. B. Savage and D. J. Jeffrey, "The stress tensor in a granular flow at high shear rates," *J. Fluid Mech.* **110**, 255–272 (1981).
- <sup>10</sup>P. Jop, Y. Forterre, and O. Pouliquen, "A constitutive law for dense granular flows," *Nature* **441**(7094), 727–730 (2006).
- <sup>11</sup>P. V. Dsouza and P. R. Nott, "A non-local constitutive model for slow granular flow that incorporates dilatancy," *J. Fluid Mech.* **888**, R3 (2020).
- <sup>12</sup>P. Jop, Y. Forterre, and O. Pouliquen, "Crucial role of sidewalls in granular surface flows: Consequences for the rheology," *J. Fluid Mech.* **541**, 167–192 (2005).
- <sup>13</sup>F. da Cruz, S. Emam, M. Prochnow, J.-N. Roux, and F. Chevoir, "Rheophysics of dense granular materials: Discrete simulation of plane shear flows," *Phys. Rev. E* **72**(2), 021309 (2005).
- <sup>14</sup>L. Sarno, Y.-C. Tai, Y. Wang, and M. Oberlack, "A well-posed multilayer model for granular avalanches with  $\mu(I)$  rheology," *Phys. Fluids* **33**(10), 103319 (2021).
- <sup>15</sup>R. Maurin, J. Chauchat, and P. Frey, "Dense granular flow rheology in turbulent bedload transport," *J. Fluid Mech.* **804**, 490–512 (2016).
- <sup>16</sup>W. Chèvrement, B. Chareyre, and H. Bodiguel, "Quantitative study of the rheology of frictional suspensions: Influence of friction coefficient in a large range of viscous numbers," *Phys. Rev. Fluids* **4**(6), 064302 (2019).
- <sup>17</sup>S. Gallier, E. Lemaire, F. Peters, and L. Lobry, "Rheology of sheared suspensions of rough frictional particles," *J. Fluid Mech.* **757**, 514–549 (2014).
- <sup>18</sup>F. Boyer, É. Guazzelli, and O. Pouliquen, "Unifying suspension and granular rheology," *Phys. Rev. Lett.* **107**(18), 188301 (2011).
- <sup>19</sup>R. Möbius and C. Heussinger, "(Ir)reversibility in dense granular systems driven by oscillating forces," *Soft Matter* **10**(27), 4806–4812 (2014).
- <sup>20</sup>L. Guan, L. Tian, M. Hou, and Y. Han, "Dynamics of a vibration-driven single disk," *Sci. Rep.* **11**(1), 16561 (2021).
- <sup>21</sup>S. S. Hsiau, M. H. Wu, and C. H. Chen, "Arching phenomena in a vibrated granular bed," *Powder Technol.* **99**(2), 185–193 (1998).
- <sup>22</sup>S. Warr, J. M. Huntley, and G. T. H. Jacques, "Fluidization of a two-dimensional granular system: Experimental study and scaling behavior," *Phys. Rev. E* **52**(5), 5583–5595 (1995).
- <sup>23</sup>H. Cai, C. Sun, S. Qin, and G. Miao, "Absolute zero' temperature in a vertically vibrated granular system," *Phys. Fluids* **35**(3), 033301 (2023).
- <sup>24</sup>T. W. Martin, J. M. Huntley, and R. D. Wildman, "Hydrodynamic model for a vibrofluidized granular bed," *J. Fluid Mech.* **535**, 325–345 (2005).
- <sup>25</sup>L.-S. Lu and S.-S. Hsiau, "Mixing in a vibrated granular bed: Diffusive and convective effects," *Powder Technol.* **184**(1), 31–43 (2008).
- <sup>26</sup>S. S. Hsiau, L. S. Lu, and C. H. Tai, "Experimental investigations of granular temperature in vertical vibrated beds," *Powder Technol.* **182**(2), 202–210 (2008).
- <sup>27</sup>P. Eshuis, K. van der Weele, D. van der Meer, and D. Lohse, "Granular Leidenfrost effect: Experiment and theory of floating particle clusters," *Phys. Rev. Lett.* **95**(25), 258001 (2005).
- <sup>28</sup>R. Caitano, B. V. Guerrero, R. E. R. González, I. Zuriguel, and A. Garcimartín, "Characterization of the clogging transition in vibrated granular media," *Phys. Rev. Lett.* **127**(14), 148002 (2021).
- <sup>29</sup>N. Gaudel and S. Kiesgen De Richter, "Effect of vibrations on granular material flows down an inclined plane using DEM simulations," *Powder Technol.* **346**, 256–264 (2019).
- <sup>30</sup>P. Eshuis, K. van der Weele, D. van der Meer, R. Bos, and D. Lohse, "Phase diagram of vertically shaken granular matter," *Phys. Fluids* **19**(12), 123301 (2007).
- <sup>31</sup>K. Zhang, H. Zhong, F. Kou, Y. Chen, and Y. Gao, "Dissipation behaviors of suspended granular balls in a vibrated closed container," *Powder Technol.* **399**, 117158 (2022).
- <sup>32</sup>C. R. K. Windows-Yule, A. D. Rosato, D. J. Parker, and A. R. Thornton, "Maximizing energy transfer in vibrofluidized granular systems," *Phys. Rev. E* **91**(5), 052203 (2015).
- <sup>33</sup>H. Cai and G. Miao, "Resonant phenomena and mechanism in vibrated granular systems," *Phys. Rev. E* **101**(3), 032902 (2020).
- <sup>34</sup>L. Li, P. Wu, S. Zhang, and L. Wang, "Vertical separation criterion of binary particles under external excitation," *Powder Technol.* **342**, 404–408 (2019).
- <sup>35</sup>C.-C. Liao, "Multisized immersed granular materials and bumpy base on the Brazil nut effect in a three-dimensional vertically vibrating granular bed," *Powder Technol.* **288**, 151–156 (2016).
- <sup>36</sup>L. Li, P. Wu, L. Wang, S. Zhang, and Z. Xie, "Patterns of convection and distribution of binary particles under vibration and airflow," *Phys. Fluids* **34**(11), 113308 (2022).
- <sup>37</sup>Y. Zhao, W. Wang, Y. Luo, Z. Liu, T. Liang, and D. Ling, "Flow regimes detection in a quasi-2D granular chute flow based on PTV technique," *Powder Technol.* **403**, 117411 (2022).
- <sup>38</sup>J. Song, H. Yang, R. Li, Q. Chen, Y. J. Zhang, Y. J. Wang, and P. Kong, "Improved PTV measurement based on Voronoi matching used in hopper flow," *Powder Technol.* **355**, 172–182 (2019).
- <sup>39</sup>B. Kou, Y. Cao, J. Li, C. Xia, Z. Li, H. Dong, A. Zhang, J. Zhang, W. Kob, and Y. Wang, "Granular materials flow like complex fluids," *Nature* **551**(7680), 360–363 (2017).
- <sup>40</sup>Z. Wang, Y. Teng, and M. Liu, "A semi-resolved CFD-DEM approach for particulate flows with kernel based approximation and Hilbert curve based searching strategy," *J. Comput. Phys.* **384**, 151–169 (2019).
- <sup>41</sup>F. Wéry, L. A. Vandewalle, G. B. Marin, G. J. Heynderickx, and K. M. Van Geem, "Hydrodynamic CFD-DEM model validation in a gas-solid vortex unit," *Chem. Eng. J.* **455**, 140529 (2023).
- <sup>42</sup>T. Eppinger, K. Seidler, and M. Kraume, "DEM-CFD simulations of fixed bed reactors with small tube to particle diameter ratios," *Chem. Eng. J.* **166**(1), 324–331 (2011).
- <sup>43</sup>Z. Xie, S. Wang, and Y. Shen, "A novel hybrid CFD-DEM method for high-fidelity multi-resolution modelling of cross-scale particulate flow," *Chem. Eng. J.* **455**, 140731 (2023).
- <sup>44</sup>O. Ayeni, S. S. Tiwari, C. Wu, J. B. Joshi, and K. Nandakumar, "Behavior of particle swarms at low and moderate Reynolds numbers using computational fluid dynamics—discrete element model," *Phys. Fluids* **32**(7), 073304 (2020).
- <sup>45</sup>S. Xiong, S. Chen, M. Zang, and T. Makoto, "Development of an unresolved CFD-DEM method for interaction simulation between large particles and fluids," *Int. J. Comput. Methods* **18**(10), 2150047 (2021).
- <sup>46</sup>L. Zhou and Y. Zhao, "Improvement of unresolved CFD-DEM by velocity field reconstruction on unstructured grids," *Powder Technol.* **399**, 117104 (2022).
- <sup>47</sup>J. Mao, L. Zhao, X. Liu, and Y. Di, "A resolved CFDEM algorithm based on the immersed boundary for the simulation of fluid-solid interaction," *Powder Technol.* **374**, 290–303 (2020).
- <sup>48</sup>Z. Shen, G. Wang, D. Huang, and F. Jin, "A resolved CFD-DEM coupling model for modeling two-phase fluids interaction with irregularly shaped particles," *J. Comput. Phys.* **448**, 110695 (2022).
- <sup>49</sup>H. Xiong, Y. Chen, M. Chen, H. Cheng, C. Yu, and J. Xiao, "Resolved CFD-DEM simulation on hydrodynamic bridging in a bend rectangle channel," *J. Braz. Soc. Mech. Sci. Eng.* **43**(7), 362 (2021).
- <sup>50</sup>W.-L. Ren, X.-H. Zhang, Y. Zhang, and X.-B. Lu, "Investigation of motion characteristics of coarse particles in hydraulic collection," *Phys. Fluids* **35**(4), 043322 (2023).
- <sup>51</sup>S. Haeri and J. S. Shrimpton, "On the application of immersed boundary, fictitious domain and body-conformal mesh methods to many particle multiphase flows," *Int. J. Multiphase Flow* **40**, 38–55 (2012).
- <sup>52</sup>R. Glowinski, T.-W. Pan, T. I. Hesla, D. D. Joseph, and J. Periaux, "A distributed Lagrange multiplier/fictitious domain method for the simulation of flow around moving rigid bodies: Application to particulate flow," *Comput. Methods Appl. Mech. Eng.* **184**(2), 241–267 (2000).
- <sup>53</sup>Z. Yu and X. Shao, "A direct-forcing fictitious domain method for particulate flows," *J. Comput. Phys.* **227**(1), 292–314 (2007).
- <sup>54</sup>N. A. Patankar, P. Singh, D. D. Joseph, R. Glowinski, and T.-W. Pan, "A new formulation of the distributed Lagrange multiplier/fictitious domain method for particulate flows," *Int. J. Multiphase Flow* **26**(9), 1509–1524 (2000).
- <sup>55</sup>S. Chen and G. D. Doolen, "Lattice Boltzmann method for fluid flows," *Annu. Rev. Fluid Mech.* **30**(1), 329–364 (1998).
- <sup>56</sup>H. Zhang, Y. Tan, S. Shu, X. Niu, F. X. Trias, D. Yang, H. Li, and Y. Sheng, "Numerical investigation on the role of discrete element method in combined LBM-IBM-DEM modeling," *Comput. Fluids* **94**, 37–48 (2014).

- <sup>57</sup>T. Wang, F. Zhang, J. Furtney, and B. Damjanac, “A review of methods, applications and limitations for incorporating fluid flow in the discrete element method,” *J. Rock Mech. Geotech. Eng.* **14**(3), 1005–1024 (2022).
- <sup>58</sup>F. Lominé, L. Scholtès, L. Sibille, and P. Poullain, “Modeling of fluid–solid interaction in granular media with coupled lattice Boltzmann/discrete element methods: Application to piping erosion,” *Int. J. Numer. Anal. Methods Geomech.* **37**(6), 577–596 (2013).
- <sup>59</sup>G. C. Yang, L. Jing, C. Y. Kwok, and Y. D. Sobral, “A comprehensive parametric study of LBM-DEM for immersed granular flows,” *Comput. Geotech.* **114**, 103100 (2019).
- <sup>60</sup>A. Hager, C. Kloss, S. Pirker, and C. Goniva, “Parallel resolved open source CFD-DEM: Method, validation and application,” *J. Comput. Multiphase Flows* **6**(1), 13–27 (2014).
- <sup>61</sup>S. Sinha, A. Garg, and H. Larochelle, in *Proceedings of the 34th International Conference on Neural Information Processing Systems* (Curran Associates Inc., Red Hook, 2020), pp. 21653–21664.
- <sup>62</sup>B.-H. Chen, Y.-S. Tseng, and J.-L. Yin, “Gaussian-adaptive bilateral filter,” *IEEE Signal Process. Lett.* **27**, 1670–1674 (2020).
- <sup>63</sup>H. Che, C. O’Sullivan, A. Sufian, and E. R. Smith, “A novel CFD-DEM coarse-graining method based on the Voronoi tessellation,” *Powder Technol.* **384**, 479–493 (2021).
- <sup>64</sup>Z. Shen, M. Wang, Y. Zeng, and F. Wang, “Optimal interpolation of spatially discretized geodetic data,” *Bull. Seismol. Soc. Am.* **105**(4), 2117–2127 (2015).
- <sup>65</sup>E. A. Lazar, J. Lu, and C. H. Rycroft, “Voronoi cell analysis: The shapes of particle systems,” *Am. J. Phys.* **90**(6), 469–480 (2022).
- <sup>66</sup>C. H. Rycroft, G. S. Grest, J. W. Landry, and M. Z. Bazant, “Analysis of granular flow in a pebble-bed nuclear reactor,” *Phys. Rev. E* **74**(2), 021306 (2006).
- <sup>67</sup>A. Panaitescu and A. Kudrolli, “Epitaxial growth of ordered and disordered granular sphere packings,” *Phys. Rev. E* **90**(3), 032203 (2014).
- <sup>68</sup>N. Guo and J. Zhao, “Local fluctuations and spatial correlations in granular flows under constant-volume quasistatic shear,” *Phys. Rev. E* **89**(4), 042208 (2014).
- <sup>69</sup>A. Hager, “CFD-DEM on multiple scales: An extensive investigation of particle-fluid interactions,” Ph.D. dissertation (Johannes Kepler University Linz, 2014).
- <sup>70</sup>E. Yazdani and S. Hassan Hashemabadi, “Three-dimensional heat transfer in a particulate bed in a rotary drum studied via the discrete element method,” *Particuology* **51**, 155–162 (2020).
- <sup>71</sup>A. A. Shirgaonkar, M. A. MacIver, and N. A. Patankar, “A new mathematical formulation and fast algorithm for fully resolved simulation of self-propulsion,” *J. Comput. Phys.* **228**(7), 2366–2390 (2009).
- <sup>72</sup>K. I. Aycok, R. L. Campbell, K. B. Manning, and B. A. Craven, “A resolved two-way coupled CFD/6-DOF approach for predicting embolus transport and the embolus-trapping efficiency of IVC filters,” *Biomech. Model. Mechanobiol.* **16**(3), 851–869 (2017).
- <sup>73</sup>C. H. Rycroft, “VORO++: A three-dimensional Voronoi cell library in C++,” *Chaos* **19**(4), 041111 (2009).
- <sup>74</sup>T. Yachai, I. Preechawuttipong, and P. Jongchansitto, in *Recent Advances in Manufacturing Engineering and Processes*, edited by R. K. Agarwal (Springer Nature, Singapore, 2023), pp. 127–134.
- <sup>75</sup>P. Mayeli and G. J. Sheard, “Buoyancy-driven flows beyond the Boussinesq approximation: A brief review,” *Int. Commun. Heat Mass Transfer* **125**, 105316 (2021).